

NOTICE: This is the author's version of a work that was accepted for publication in Computers & Geotechnics. Changes resulting from the publishing process, such as peer review, editing, corrections, structural formatting, and other quality control mechanisms may not be reflected in this document. Changes may have been made to this work since it was submitted for publication. A definitive version was subsequently published in Computers & Geotechnics, 146:104677, 2022. doi: 10.1016/j.compgeo.2022.104677

Mortar contact discretisation methods incorporating interface models based on Hypoplasticity and Sanisand: application to vibratory pile driving

Patrick Staubach^{*}; Jan Machaček[†]; Torsten Wichtmann[‡]

Abstract: A segment-based mortar contact discretisation technique for the analysis of hydro-mechanically coupled dynamic processes with quadratically interpolated finite elements and incorporating advanced interface models is presented. The proposed mortar technique divides the surface pair into finite segments with arbitrary order of integration, allowing, opposite to simpler contact discretisation techniques, for an exact integration of contact stress. The performance of the segment-based in comparison to a (simpler) element-based mortar technique is evaluated by means of simulations of vibratory pile driving model tests in water-saturated sand. For the mechanical modelling of the soil-pile interface either a simple Coulomb friction model, the hypoplastic model with intergranular strain extension, or the elastoplastic Sanisand model is utilised. It is concluded that the segment-based mortar method is superior to the element-based technique in terms of numerical stability if the number of integration points per segment is larger than the number of integration points per element edge for the element-based technique. However, the techniques are found to perform similarly when a comparable number of integration points is used. While the implementation of the segment-based method is found to be more complex in general, the implementation of parallelisation is simpler compared to the element-based mortar method.

Keywords: mortar method; contact mechanics; vibratory pile driving; hydro-mechanically coupled; Hypoplasticity; Sanisand

1 Introduction

The numerical analysis of vibratory pile driving in water-saturated soil is a challenging task. There exist a few numerical studies, which often simplify the physical processes strongly (e.g. only ideally drained/ideally undrained conditions, no consideration of friction between pile and soil, application of constitutive models not suitable for cyclic loading or no consideration of inertia (Grabe and Mahutka, 2005; Osinov et al., 2013; Osinov, 2015; Chrisopoulos et al., 2016; Chrisopoulos, 2018; Staubach and Machaček, 2019; Daryaei et al., 2020). Recently, the numerical analysis of pile installation processes has received more attention (Henke and Grabe, 2008; Henke, 2010; Henke, 2014; Galavi et al., 2019;

^{*}Chair of Soil Mechanics, Foundation Engineering and Environmental Geotechnics, Ruhr Universität Bochum, Germany/Chair of Geotechnics, Bauhaus Universität Weimar, Germany. Email: patrick.staubach@rub.de, Corresponding author

[†]Institute of Geotechnics, Technische Universität Darmstadt, Germany/Chair of Soil Mechanics, Foundation Engineering and Environmental Geotechnics, Ruhr-Universität Bochum, Germany

[‡]Chair of Soil Mechanics, Foundation Engineering and Environmental Geotechnics, Ruhr-Universität Bochum, Germany

9 Moormann et al., 2019; Heins et al., 2020; Staubach et al., 2020; Yang et al., 2020; Bienen et al., 2021;
10 Fan et al., 2021; Le et al., 2021; Soleimani and Weissenfels, 2021), partly driven by the interest of the
11 offshore wind industry in evaluating the influence of different installation techniques on the performance
12 of offshore foundations.

13 For the numerical analysis of pile driving many challenging aspects of computational geomechanics
14 are combined. Those are namely large-deformations of the soil, contact constraints between pile and soil,
15 hydro-mechanically coupled processes and (high frequency) dynamics in case of impact and vibratory pile
16 driving. The numerical treatment of the contact constraints, including the discretisation of the contacts,
17 the enforcement of the contact constraints and the constitutive description of the interface subjected
18 to shearing, is of particular importance to obtain reliable numerical results (Sheng et al., 2005; Fischer
19 et al., 2007). Due to cyclic interface shearing in case of impact or vibratory pile driving, the constitutive
20 interface models utilised should be able to reproduce the soil response to cyclic loading. Numerically
21 stable contact modelling techniques capable to take into account large-deformations are required for the
22 simulation of pile installation, which places high demands on the numerical code used. Even though being
23 directly linked, most research work has either focused on the continuum mechanical aspects of contact
24 mechanics (i.e. discretisation of the contacts and enforcement of constraints) or the geomechanical aspects
25 (i.e. constitutive interface behaviour).

26 One of the most advanced family of contact discretisation techniques are the so-called mortar methods.
27 In general, mortar techniques can be divided into *segment-based* (Puso and Laursen, 2004; Yang et
28 al., 2005; Puso et al., 2008; Popp et al., 2009) and *element-based* (Fischer and Wriggers, 2005; Fischer
29 and Wriggers, 2006; Tur et al., 2009) mortar techniques (Farah et al., 2015). In the framework of the
30 segment-based mortar technique, the surfaces of the contact pair are divided in finite segments, which
31 are interpolated and integrated similar as continuum finite elements (no discrete contact elements are
32 introduced, however). In contrast, the element-based mortar technique does not require the segmentation
33 of the surface pair and uses the integration points (existing or potentially additionally created) of the
34 edges/surfaces of the underlying finite elements for the surface integration, analogous to the integration
35 of regular (constant) external tractions.

36 Opposite to simpler contact discretisation techniques (e.g. the Node-to-Surface (NTS) method imple-
37 mented in many finite element codes), both mortar techniques satisfy contact patch tests used to evaluate
38 the performance of the contact discretisation technique (El-Abbasi and Bathe, 2001). The Babuška-Brezzi
39 stability requirements can be satisfied as well (Wohlmuth, 2001). In addition, determination and integra-
40 tion of the contact stresses using mortar methods is in general not (strongly) dependent on the discreti-
41 sation of the underlying continuum and the methods are suitable for large-deformation analyses. Mortar
42 methods allow for a local refinement of the geometry of the contacting surfaces, resulting in a smoother
43 distribution of contact stresses compared to simpler contact discretisation techniques. A refinement is in
44 particular appealing for the incorporation of state-dependent constitutive interface models, such as used
45 for soils. This is due to their sensitivity towards small changes in strain (in particular changes of strain
46 direction) caused by (spatially) discontinuous relative surface movements and jumps in contact stresses
47 using less advanced contact discretisation techniques. Furthermore, using quadratically interpolated finite
48 elements, as often applied in computational geomechanics, is troublesome in combination with the NTS
49 method (Wriggers, 2006b), whereas such limitations are not faced using mortar methods.

50 A 2D large-deformation segment-based mortar contact discretisation technique is presented in this work.
51 It allows to consider sophisticated friction models and is suitable for quadratically interpolated finite ele-
52 ments. The state-dependency of the friction model such as necessary for a hypoplastic or a Sanisand inter-
53 face model is considered. The mortar contact discretisation technique is applied for the large-deformation
54 analysis of vibratory pile driving in water-saturated soil considering friction and strongly non-linear con-
55 stitutive (interface) models. Compared to existing work, these simulations add complexity not only due
56 to the additional non-linearities but also because of non-conforming meshes (i.e. differing element sizes
57 of the paired surfaces) with frequently changing node connectivities due to the large penetration depth
58 of the pile during the installation process.

59 The proposed segment-based mortar method is compared to an element-based mortar technique. Both

60 schemes are implemented in the in-house finite element code `numgeo`¹ developed by the first two authors.

61 2 Mortar contact discretisation

62 Mortar methods have originally been proposed for the decomposition of domains and were only later
63 applied to contact mechanics. The first application of the mortar technique as contact discretisation
64 method was reported by (Simo et al., 1985; Zavarise and Wriggers, 1998; Papadopoulos and Taylor, 1992).
65 These early versions of the mortar technique have then been extended by (Puso and Laursen, 2004; Yang et
66 al., 2005) to allow for frictional contact and consideration of large-deformations for 2D applications. (Yang
67 and Laursen, 2008) later developed a mortar method for self contact (i.e. a body coming into contact with
68 itself) taking into account large-deformations as well. (Puso et al., 2008) presented a 3D mortar method
69 and an extension for quadratically interpolated finite elements. (Tur et al., 2009) developed an element-
70 based mortar approach for 2D using Lagrange multipliers including frictional forces. The division of the
71 surfaces into segments is not required, which saves computational time and makes the implementation
72 more straightforward. A comparison of segment-based vs. element-based integration in the framework of
73 the mortar method has been presented by (Farah et al., 2015), concluding that the segment-based method
74 can be slightly more accurate. (Popp, 2012) developed a mortar contact technique for fluid-structure
75 interfaces using dual Lagrange multipliers (Popp et al., 2010), allowing for static condensation of the
76 additional unknowns introduced by the Lagrange multiplier. In (Sitzmann, 2016) the implementation of
77 the mortar method in the open-source finite element code `Calculix`² has been presented. (Farah et al.,
78 2018) proposed a 3D mortar method for refined analysis of sharp corners and edges. An overview over
79 proposed mortar contact techniques can be found in (Laursen et al., 2012). In all of the aforementioned
80 work the mortar contact discretisation has been used for classical solid mechanics applications such as
81 ironing. Early applications of mortar methods in geomechanics are reported e.g. in (Fischer et al., 2007). In
82 more recent work, mortar methods have also been used in combination with hydro-mechanically coupled
83 finite elements considering partially drained conditions (Sabetamal et al., 2016b; Sabetamal et al., 2016a).
84 In addition, the analysis of unsaturated soils employing mortar contact techniques has been reported in
85 (Ghorbani et al., 2021).

86 The novel aspects of this paper compared to the aforementioned works are in particular:

- 87 • Evaluation of segment-based vs. element-based mortar techniques for complex geotechnical instal-
88 lation processes with large relative surface movements including friction
- 89 • Incorporation of advanced constitutive interface models in both mortar techniques

90 2.1 Contact kinematics

91 In the framework of mortar methods, the paired surfaces are often referred to as the mortar and the
92 non-mortar side. In this work, however, we stick to the classical convention, where one surface of the
93 contact pair is denoted as the slave ($\square^{(1)}$) (i.e. the surface with the finer mesh) and the other as master
94 ($\square^{(2)}$) surface. The gap \mathbf{g} between the surfaces is calculated using

$$\mathbf{g} = \mathbf{X}^{(1)} + \mathbf{u}^{(1)} - (\mathbf{X}^{(2)} + \mathbf{u}^{(2)}) = \mathbf{g}_0 + \mathbf{u}^{(1)} - \mathbf{u}^{(2)}, \quad (1)$$

95 where \mathbf{g}_0 is the gap in the reference configuration and $\mathbf{u}^{(i)}$ ($i = \{1, 2\}$) is the displacement of the slave
96 and the master node, respectively. $\mathbf{X}^{(i)}$ is the spatial coordinate in the reference configuration of the slave

¹`numgeo` (Machaček & Staubach, see (Machaček, 2020; Machaček and Staubach, 2021; Machaček et al., 2021b; Staubach et al., 2021a; Staubach et al., 2022b; Staubach et al., 2021c; Staubach et al., 2021b; Staubach et al., 2022a) and www.numgeo.de) is a stand-alone finite element program developed by the first two authors for the solution of non-linear, coupled (dynamic) geotechnical boundary value problems.

²`Calculix` is a finite element code for structural mechanics applications. The interested reader is referred to www.calculix.de.

97 and the master node, respectively. The contact gap has a normal

$$\mathbf{g}_N = \mathbf{n}^{(2)} \otimes \mathbf{n}^{(2)} \cdot \mathbf{g} \quad (2)$$

98 and a tangential component

$$\mathbf{g}_T = (\mathbf{I} - \mathbf{n}^{(2)} \otimes \mathbf{n}^{(2)}) \cdot \mathbf{g}. \quad (3)$$

99 Therein $\mathbf{n}^{(2)} = -\mathbf{n}^{(1)}$ is the normal vector of the master surface and $\mathbf{I} = \text{diag}[1, 1, 1]$. $\mathbf{n}^{(1)}$ is the normal
100 vector of the slave surface. Similar to the gap, the contact stress vector of the contact pair can be separated
101 in its normal and tangential components, viz.

$$\mathbf{t} = \mathbf{t}_N + \mathbf{t}_T. \quad (4)$$

102 The tangential stress vector is defined by

$$\mathbf{t}_T = \mathbf{t} - \mathbf{t}_N = (\mathbf{I} - \mathbf{n}^{(2)} \otimes \mathbf{n}^{(2)}) \cdot \mathbf{t}. \quad (5)$$

103 The scalar normal gap component g_N is calculated using

$$g_N = \mathbf{n}^{(1)} \cdot \mathbf{g} = -\mathbf{n}^{(2)} \cdot \mathbf{g} \quad (6)$$

104 and the scalar normal contact stress component t_N (negative for compression) by

$$t_N = \mathbf{n}^{(1)} \cdot \mathbf{t} = -\mathbf{n}^{(2)} \cdot \mathbf{t}. \quad (7)$$

105 The (total) normal stress can be decomposed according to Terzaghi's principle in

$$t_N = t'_N - p^w, \quad (8)$$

106 where the effective normal stress t'_N and the pore water pressure p^w (positive for compression) are in-
107 troduced. Conventionally, the contact pair has to satisfy the following conditions (known as the *Karush-*
108 *Kuhn-Tucker* conditions):

- 109 • Only contact pressure is possible $t_N \leq 0$
- 110 • A penetration is not allowed $g_N \geq 0$
- 111 • *Complementary condition* enforcing $g_N t_N = 0$

112 In this work, the first and last condition are not enforced, since in water-saturated soil, the pile can
113 not separate from the water as long as no cavitation takes place allowing for positive values of t_N (and
114 non-zero normal contact stress despite $g_N > 0$). This means that for positive values of g_N , the effective
115 stress component t'_N is zero and the pore water pressure p^w takes negative values. Thus, $t_N = -p^w$ holds
116 in this case. As is elaborated on in a later section, a \mathbf{u} -p finite element formulation is used for the spatial
117 discretisation of the continuum in this work (the arising linear system is solved for the solid displacements
118 \mathbf{u} and the pore water pressure p^w (Zienkiewicz and Shiomi, 1984)). The no-separation condition is taken
119 into account by enforcing the displacements of the pile and the displacements of the solid phase of the soil
120 to be identical at the interface in normal direction to it. The penalty regularisation is used for this purpose.
121 Note that in (Sorensen et al., 2017) the enforcement of no-separation conditions has been investigated
122 for different hydro-mechanically coupled finite element formulations discretising the fluid displacement
123 in addition (\mathbf{u} -p- \mathbf{U} elements), only enforcing the fluid displacement to be identical at the interface. The
124 solid displacement was not directly constrained at the interface in this case. For the quasi-static analyses
125 presented in (Sorensen et al., 2017), no significant differences between the present approach using \mathbf{u} -p
126 elements (coupling the solid displacement) and the \mathbf{u} -p- \mathbf{U} elements (coupling only the fluid displacement
127 with the displacement of the structure) were found, justifying the approach used in this work.

128 All finite element operations required for the discretisation of the continuum as well as the spatially
 129 discretised balance equations are defined in Appendix A.

130 2.2 Evaluation of the convective coordinate

131 Prior to the *segmentation* of the contact surfaces, the evaluation of the *convective coordinate* $\bar{\xi}$ is necessary.
 132 Based on the node-to-node connectivity evaluated using the Euclidean norm, the minimum distance
 133 between the master and the slave surface is calculated using the convective coordinate $\bar{\xi}$ (taking values
 134 from -1 to 1). First, an orthogonal projection of the coordinates $\mathbf{x}_I^{(1)}$ of slave node I onto the master
 135 surface $\Gamma_c^{(2)}$ is performed. This is done by enforcing the (non-normalised) tangential vector of the master
 136 surface $\mathbf{x}_{,\xi}^{(2)}(\bar{\xi}^{(2)})$ to be orthogonal to the normal gap vector with minimum magnitude between the master
 137 surface and slave node I . The projection is defined by

$$\left[\sum_J^{\text{nnode}} N_J^{(2)}(\bar{\xi}^{(2)}) \mathbf{x}_J^{(2)} - \mathbf{x}_I^{(1)} \right] \cdot \mathbf{x}_{,\xi}^{(2)}(\bar{\xi}^{(2)}) \stackrel{!}{=} 0, \quad (9)$$

138 yielding $\bar{\xi}^{(2)}$.

139 As proposed in (Yang et al., 2005), the projection is always performed using the (non-normalised)
 140 tangential vector at the master surface and not using the tangential vector at the slave and master
 141 surface, respectively. This is advantageous for the definitions of the segments as is demonstrated in Fig.
 142 1. Figure 1a shows the determination of the segments using a definition of the convective coordinate
 143 where the tangential vector at both surfaces is used. As is indicated, some surface area at the blue slave
 144 surface of the green segment on the left-hand side is lost. The improved evaluation of the convective
 145 coordinate evaluating the tangential vectors only at the master surface (displayed in Fig. 1b) avoids this
 146 shortcoming. The convective coordinate of the slave surface $\bar{\xi}^{(1)}$ is thus calculated using

$$\left[\sum_I^{\text{nnode}} N_I^{(1)}(\bar{\xi}^{(1)}) \mathbf{x}_I^{(1)} - \mathbf{x}_J^{(2)} \right] \cdot \mathbf{x}_{J,\xi}^{(2)} \stackrel{!}{=} 0. \quad (10)$$

147 Note that the to node J connected nodes with the label I (and vice versa for Eq. (9)) are based on an
 148 initial screening of the surface pair using the euclidean norm to find the shortest distances.

149 During the minimisation of Eqs. (9, 10) the local coordinate may exceed the boundaries of the under-
 150 lying continuum element ($\{\|\bar{\xi}\| > 1\}$). In this case, the minimisation has to continue with the edge of the
 151 next continuum element to which the local coordinate points.

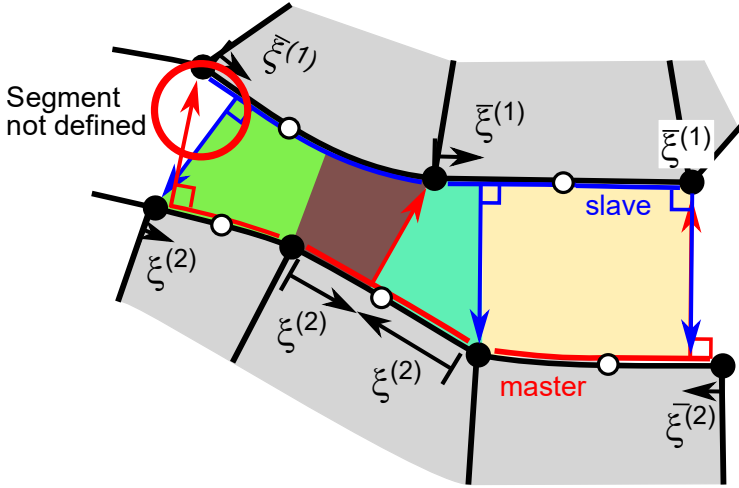
152 Fig. 1b also shows the case of two convective coordinates for one node (being the case for the slave node
 153 between the brown and aquamarine segment in the centre of the slave surface). This additional projection
 154 (*correction projection*) is required, if no projection is performed to a master node (the master node at
 155 the brown segment in Fig. 1a). Note that the lost surface area of the master surface on the far right-hand
 156 side of Fig. 1b would not occur in the actual analysis, as long as the hinted slave element on the far
 157 right-hand side would be included in the slave surface definition. If this element edge is not included in
 158 the surface definition, the surface area of the master surface would be lost, since no orthogonal projection
 159 to the master node on the far right-hand side is possible.

160 2.3 Segmentation

161 Having determined the convective coordinates of both surfaces, the division of the contacting surfaces
 162 into finite segments, analogous to the division of a continuum in finite elements, has to be performed.
 163 This subdivision of the surfaces into segments is beneficial, because it allows to exactly determine and
 164 integrate the contact stress with a possibility of a locally refined spatial discretisation of the contact
 165 surfaces.

166 As displayed in Fig. 2, six different types of segments are identified, which differ in the way the borders

a) "Conventional" projection



b) Improved projection

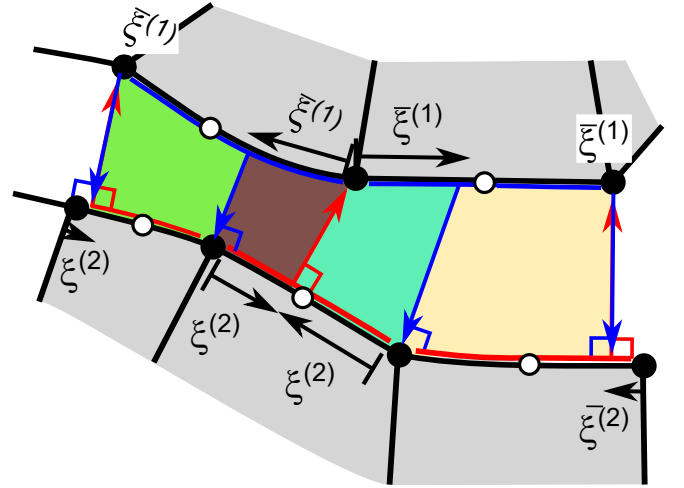


Figure 1: Contact discretisation using the segment-based mortar approach. a) Segmentation using the conventional projection scheme with normal vectors evaluated alongside the master and the slave surface, respectively. b) Improved scheme for which the normal vectors are evaluated only at the master surface using Eqs. (9, 10). The segments after evaluation of the convective coordinates are depicted as well.

167 of the segment are defined. The border of a segment is either an existing node or the value of the convective
 168 coordinate $\bar{\xi}^{(i)}$. Note that the segment is always defined according to the nodes and convective coordinates
 169 at the slave surface, i.e. in Fig. 2 the criteria defining the type of segment refer to the convective coordinate
 170 evaluated at the slave surface. In case of the segment type I for instance, both convective coordinates
 171 of the finite element at the slave surface are outside the edge of the actual finite element. Hence, the
 172 segment is formed by two existing nodes on the slave surface. Both convective coordinates of the master
 173 surface, however, are on the same edge of the identical finite element.

174 The segment types V and VI are established by the same nodes as in case of types II and III, respectively.
 175 However, the convective coordinate for types III and V starts from the same node that forms the segment
 176 while in cases II and VI the convective coordinate of a different node is used. This distinction is only
 177 important in the context of the implementation. As proposed by (Popp, 2012), only exterior nodes are
 178 projected in case of finite elements with interpolation order two or higher. Interior nodes are not involved
 179 in the segmentation process and are located inside of the segments.

180 As stated in (Wriggers, 2006a), the segmentation can be difficult to program. In particular, if the
 181 numbers of nodes of the two surfaces differs significantly but no surface can be defined as being finer
 182 discretised for the entire contact zone, the herein adopted scheme, where the segmentation is performed
 183 based on the finer discretised surface (i.e. the slave surface), may fail. It is worth mentioning that the
 184 segmentation increases in complexity in case of 3D analyses. Special algorithms, such as the *Sutherland-*
 185 *Hodgman* polygon clipping algorithm (Sutherland and Hodgman, 1974) employed by (Sitzmann, 2016;
 186 Puso et al., 2008) or Delaunay triangulation (Hesch and Betsch, 2011) have to be applied in that case.

187 2.4 Interpolation of segments

188 The variables within each segment are interpolated using the local coordinate η , which takes values from
 189 -1 to 1, analogously to the local coordinate of regular (rectangular/brick) finite elements. The order of
 190 the interpolation function is defined according to the number of existing and projected nodes forming the
 191 segment. The mapping from the local finite element edge coordinate $\xi^{(1)}$ of the slave surface to the local
 192 coordinate of the segment formed at the slave surface in case of linear finite elements is performed by

$$\xi^{(1)}(\eta) = \frac{1}{2}(1 - \eta)\xi_a^{(1)} + \frac{1}{2}(1 + \eta)\xi_b^{(1)}, \quad (11)$$

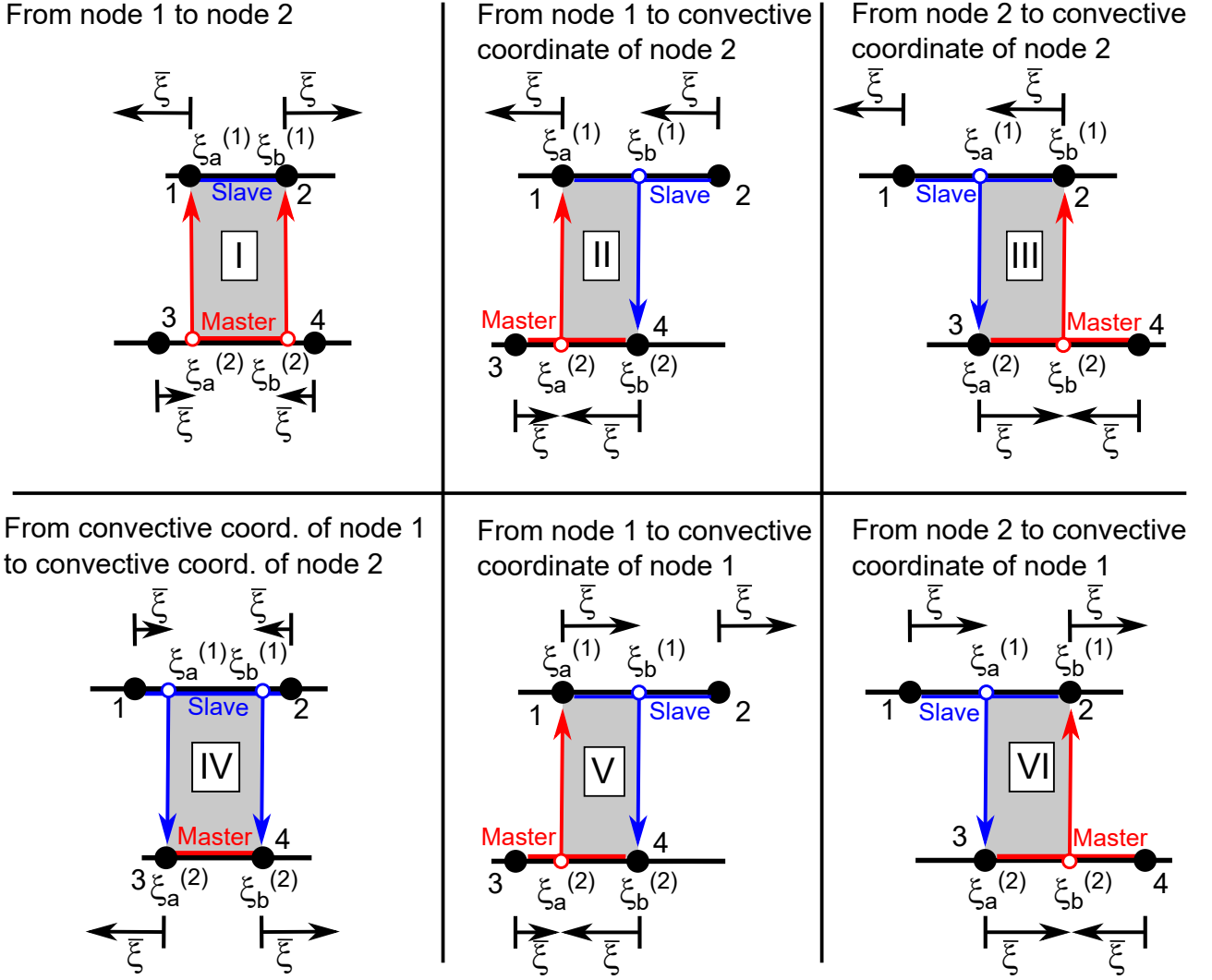


Figure 2: Definition of different types of segments in dependence of the arrangement of nodes and convective coordinates. An unfilled circle represents the location of the convective coordinate while filled dots are existing (exterior) nodes.

193 wherein $\xi_a^{(1)}$ is the first local coordinate of the segment and $\xi_b^{(1)}$ the second. As is indicated in Fig. 2,
 194 $\xi_a^{(1)}$ and $\xi_b^{(1)}$ can either represent projections using the convective coordinate or existing nodes. A similar
 195 interpolation rule is set up for the master side of the segment, viz.

$$\xi^{(2)}(\eta) = \frac{1}{2}(1 - \eta)\xi_a^{(2)} + \frac{1}{2}(1 + \eta)\xi_b^{(2)}. \quad (12)$$

196 In case of quadratically interpolated finite elements, the following interpolation of the local coordinate of
 197 the element with respect to the local coordinate of the segment is used

$$\xi^{(i)}(\eta) = -\frac{1}{2}\eta(1 - \eta)\xi_a^{(i)} + \frac{1}{2}\eta(1 + \eta)\xi_b^{(i)} + (1 - \eta^2)\xi_c^{(i)}, \quad (13)$$

198 wherein $\xi_c^{(i)}$ is $(\xi_a^{(i)} + \xi_b^{(i)})/2$ and $i = \{1, 2\}$.

199 As has been mentioned earlier, the contact contributions of the mortar segments can be integrated
 200 using a different order as employed for the underlying finite element. Often, a higher order of integration
 201 of the segment compared to the order of integration of the finite element is applied (Popp, 2012). This is
 202 advantageous since the distance between slave and master surface can vary strongly within one segment

203 if the mesh is coarse. For higher order of integration, the distance is calculated in more integration points
 204 of the segment thus allowing for a more precise calculation of the gap and a better approximation of the
 205 contact stress, which is often spatially irregularly distributed.

206 For each integration point igp of the segment, the coordinates $\mathbf{x}_{igp}^{(i)}$ and contact stress \mathbf{t}_{igp} are interpo-
 207 lated using

$$\mathbf{x}_{igp}^{(i)} = \sum_L^{\text{nnode}} N_L^{\text{seg}}(\eta_{igp}) \mathbf{x}_L^{(i)} \quad \text{and} \quad (14)$$

$$\mathbf{t}_{igp} = \sum_L^{\text{nnode}} N_L^{\text{seg}}(\eta_{igp}) \mathbf{t}_L. \quad (15)$$

208 η_{igp} is the local coordinate of the integration point, N^{seg} is the interpolation function of the segment, \mathbf{x}_L
 209 is the (global) coordinate of a, possible "imaginary", node L (unfilled circle in Fig. 2) and \mathbf{t}_L is the (total)
 210 contact stress vector at node L from a previous calculation step. Note that for hydro-mechanically coupled
 211 analyses, the effective normal contact stress is required for the calculation of shear stresses. Therefore,
 212 the pore water pressure p^w is interpolated from the nodes of the finite elements to the integration points
 213 of the segments to calculate the effective normal contact stress. The effective normal contact stress $t'_{N,igp}$
 214 at the integration points of the segment is defined by

$$t'_{N,igp} = t_{N,igp} + p_{igp}^w = \sum_L^{\text{nnode}} N_L^{\text{seg}}(\eta_{igp}) (t_{N,L} + p_L^w), \quad (16)$$

215 where the interpolation from the nodes introduced in Eq. (15) is used.

216 The nodes L are located at the border (at the local finite element coordinates $\xi_a^{(i)}$ and $\xi_b^{(i)}$) and, if the
 217 underlying finite element is quadratically interpolated, in the middle of the segment (at the local finite
 218 element coordinate $\xi_c^{(i)}$). They are either imaginary, if the local convective coordinate and the location
 219 of the existing finite element nodes are not identical, or identical to existing nodes I otherwise. In case
 220 of imaginary nodes, their values have to be obtained using a similar interpolation as in Eqs. (14, 15) but
 221 using the local convective coordinates $\bar{\xi}$ and the values at the existing finite element nodes I . Of course, it
 222 is also possible to directly interpolate the nodal values to the integration points of the segments without
 223 obtaining them at the borders of the segments first.

224 State variables are not saved at the integration points of the segments but at the nodes of the finite
 225 elements. The values of the integration points thus have to be obtained by interpolation from the nodes in
 226 every calculation step (i.e. every iteration) since any displacement of the surface pair changes the coordi-
 227 nates of the segments and hence the location of the integration points. Opposite to the integration points
 228 of regular finite elements, the integration points of the mortar segment are therefore not "permanent"
 229 but are newly created in every calculation step (i.e. in every iteration). Conceptually, this is similar to a
 230 (conventional) particle finite element method (PFEM) (Idelsohn et al., 2004), where the existing nodes
 231 are newly connected thereby creating a new set of integration points for which the initial state variables
 232 are obtained by interpolation using the saved values at the nodes.

233 In addition to Eqs. (14, 15), the relative tangential displacement increment is interpolated, if a fric-
 234 tional contact definition is used. If the constitutive contact model requires additional state variables, an
 235 additional interpolation is required.

236 Once the (current) global coordinates of every integration point of the slave and the master side of the
 237 segment have been calculated, the distance between the integration points is determined for each of the
 238 points using

$$\mathbf{g}_{igp} = \mathbf{x}_{igp}^{(2)} - \mathbf{x}_{igp}^{(1)}. \quad (17)$$

239 The normal and tangential component of the distance are

$$g_{N,\text{igp}} = (\mathbf{x}_{\text{igp}}^{(2)} - \mathbf{x}_{\text{igp}}^{(1)}) \cdot \mathbf{n}_{\text{igp}}^{(1)} \quad \text{and} \quad (18)$$

$$g_{T,\text{igp}} = (\mathbf{x}_{\text{igp}}^{(2)} - \mathbf{x}_{\text{igp}}^{(1)}) \cdot \boldsymbol{\tau}_{\text{igp}}^{(1)}, \quad (19)$$

240 where $\boldsymbol{\tau}_{\text{igp}}$ is the (normalised) tangential vector at the integration point. For frictional analyses, an
 241 incremental formulation is required. The increment in relative tangential movement $\Delta g_{T,\text{igp}}$ is calculated
 242 using

$$\Delta g_{T,\text{igp}} = (\Delta \mathbf{u}_{\text{igp}}^{(2)} - \Delta \mathbf{u}_{\text{igp}}^{(1)}) \cdot \boldsymbol{\tau}_{\text{igp}}^{(1)}. \quad (20)$$

243 The increment of displacement $\Delta \mathbf{u}_{\text{igp}}$ in Eq. (20) is obtained using a similar interpolation as used in Eq.
 244 (14).

245 For the integration of the segments, five integration points are used for each segment as proposed in
 246 (Yang et al., 2005; Popp, 2012). The higher integration order allows for a more refined determination of
 247 the, usually with respect to the local coordinate of the segment non-constant, distribution of the normal
 248 and tangential distances given by Eqs. (18, 19) and hence the contact stress. An integration with a larger
 249 number of integration points (seven and nine) is implemented as well. However, for typical meshes used,
 250 five integration points have proven to be a good compromise between accuracy and computational cost.
 251 As mentioned earlier, the integration points are created in every calculation step, allowing to change
 252 the number of integration points at any time of the analysis. If strongly fluctuating values and complex
 253 geometries are obtained for a segment at a certain stage of an analysis, an increase of the number of
 254 integration points during the calculation is therefore possible.

255 2.5 Contribution to the balance equations, integration and extrapolation

256 The contribution to the balance equation of linear momentum (see Eq. (35) in Appendix A) in case of
 257 active contact is

$$\mathbf{r}_I^C = \int_{\Gamma^C} \mathbf{t}_I^C d\Gamma^C, \quad (21)$$

258 wherein \mathbf{r}_I^C is the contact force at node I , Γ^C is the contact area and \mathbf{t}_I^C the total contact stress. Eq. (21)
 259 is numerically integrated for the slave ($i = 1$) and master ($i = 2$) surface using

$$\mathbf{r}_I^{C,(i)} = \sum_{\text{igp}}^{\text{ngp}} N_I^{(i)}(\xi^{(i)}(\eta_{\text{igp}})) \mathbf{t}_{\text{igp}}^{(i)} w_{\text{igp}} j_{\text{igp}}^{(i)}. \quad (22)$$

260 $N_I^{(i)}$ is the interpolation function of the edge of the finite element underlying the mortar segment for
 261 the slave and master side, respectively. It is evaluated according to the local segment coordinate of the
 262 integration point of the mortar segment. Note that the normal component of the contact stress $\mathbf{t}_{\text{igp}}^{(i)}$ is the
 263 same for the slave and the master side in magnitude, but has opposite sign. The local segment coordinate
 264 η_{igp} and the integration point weights w_{igp} are shared by the surfaces and hence no exponent indicating
 265 the slave or master surface is necessary.

266 In Eq. (22), $j_{\text{igp}}^{(i)} = \left\| \frac{\partial \mathbf{x}^{(i)}(\xi_{\text{igp}})}{\partial \xi^{(i)}} \right\| \left\| \frac{\partial \xi^{(i)}(\eta_{\text{igp}})}{\partial \eta} \right\|$ takes into account the mapping from the local to the global
 267 coordinate system. The second factor describing the change of the local element coordinate ξ with local
 268 segment coordinate η is necessary since the segment length differs from the length of the complete element

269 edge in general. $\frac{\partial \xi^{(i)}}{\partial \eta}$ yields in case of linearly interpolated elements

$$\frac{\partial \xi^{(i)}}{\partial \eta} = \frac{1}{2} (\xi_b^{(i)} - \xi_a^{(i)}) \quad (23)$$

270 and in case of quadratically interpolated elements

$$\frac{\partial \xi^{(i)}}{\partial \eta} = -\frac{1}{2}(1 - 2\eta)\xi_a^{(i)} + \frac{1}{2}(1 + 2\eta)\xi_b^{(i)} - 2\eta\xi_c^{(i)}. \quad (24)$$

271 The integration of three segments formed at the edge of the quadratically interpolated finite element
 272 *ielem* is exemplary shown in Fig. 3. The values of the interpolation functions N_I with respect to the
 273 local coordinate of *ielem* are given in the plot. The segments I, II and III are also given with their
 274 borders according to the local coordinate. Each segment has 5 integration points, which are given in
 275 blue for segment I, red for segment II and green for segment III. Their location depends on the local
 276 coordinate of the segment η . In order to demonstrate the integration of an arbitrary variable given
 277 at the integration points of the segment, a variable with identical value for every integration point is
 278 considered. Its distribution with respect to the local coordinate of the element is given by the blue line.
 279 For the integration of the variable, the interpolation functions of the three nodes of the quadratically
 280 interpolated *ielem* are evaluated at the location of the integration points of the segments using Eq. (13)
 281 and integrated using Eq. (22). The integrated values obtained at the nodes of *ielem* are given below the
 282 plot, being 0.3333 for the corner nodes and 1.3333 for the middle node. These values agree with those
 283 obtained by analytical integration of the constant variable with a value of 1 over a line length of 2. Of
 284 course, the example is only of academic nature.

285 After all contact variables (gap, stress and state variables) have been updated at the integration points
 286 of the segment, the values have to be extrapolated to the finite element nodes at which they are saved
 287 for the next calculation step. The extrapolation is performed in analogy to Eqs. (14, 15) using

$$\sqcup_L^{(i)} = \sum_{\text{igp}}^{\text{ngp}} N_{\text{igp}}^{(i)}(\eta'_L) \sqcup_{\text{igp}}^{(i)}, \quad (25)$$

288 where η'_L is the *stretched* local coordinate of the point to which the integration point values are extrapo-
 289 lated. As already explained for the interpolation given by Eqs. (14, 15), the node L is either an imaginary
 290 segment border node or an existing node of a finite element. Only in case L is an existing node ($L = I$)
 291 an extrapolation is performed and the values are saved at node I .

292 For an implicit solution scheme using the Newton-Raphson method, the partial derivatives of the
 293 contact contributions with respect to the primary variables discretised in the finite element framework are
 294 required. The analytically calculated derivatives for the segment-based mortar discretisation technique
 295 can be found in Appendix B. However, if the constitutive interface model is complex, an analytical
 296 determination of the derivatives is not straight-forward and sometimes not even possible. For such cases,
 297 a numerical differentiation scheme is used, which is described in detail in (Staubach et al., 2022c).

298 2.6 Advanced constitutive interface models based on Hypoplasticity and 299 Sanisand

300 A simple Coulomb friction model can only capture a limited number of aspects of the mechanical be-
 301 haviour of soil-structure interfaces, which has been demonstrated by experimental (Fakharian, 1996;
 302 Zhang and Zhang, 2008; Zhang and Zhang, 2009; Feng et al., 2018) and numerical (Ghionna and Mor-
 303 tara, 2002; Liu et al., 2006; Liu and Ling, 2008; Lashkari, 2012; Liu et al., 2014; Weißenfels and Wriggers,
 304 2015; Saberi et al., 2016; Stutz et al., 2016; Stutz et al., 2017; Weißenfels et al., 2017; Saberi et al., 2018;
 305 Saberi et al., 2020; Yang and Yin, 2021) investigations. Therefore, novel constitutive interface models

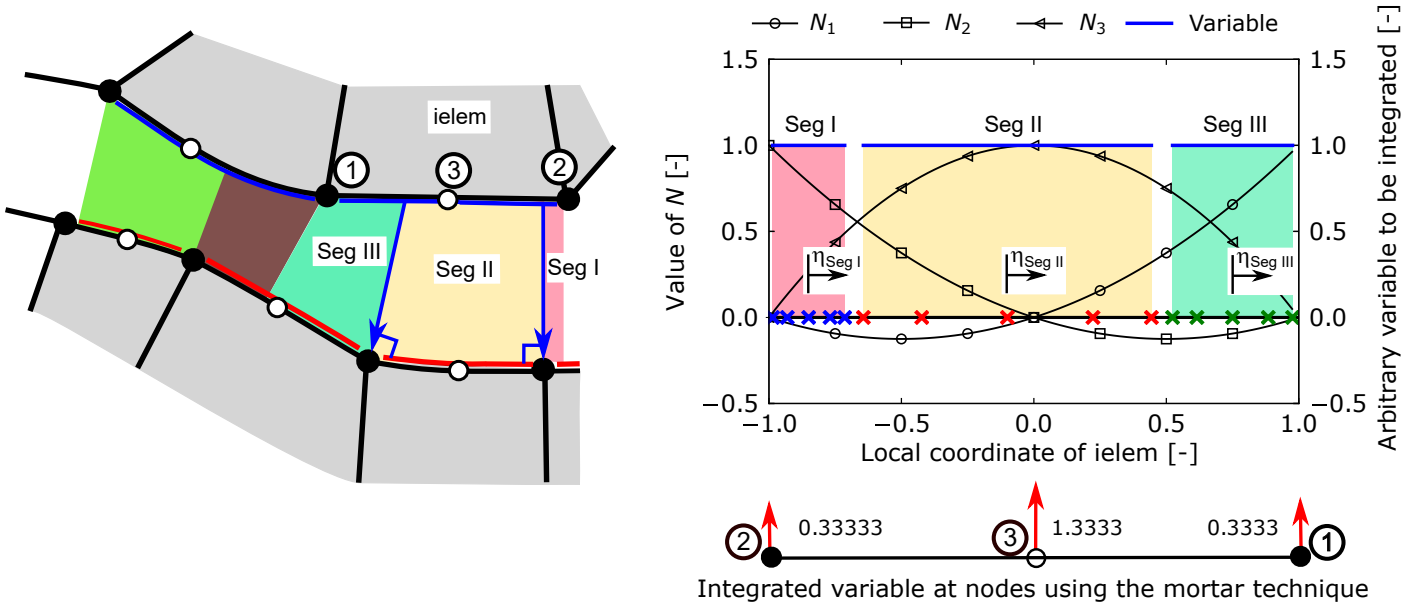


Figure 3: Example for the integration of segment variables to finite element node values. The left figure depicts the three segments at the element edge of the finite element *ielem*. The right plot shows the integration of the three segments for an exemplary distribution of an arbitrary variable given in blue. The variable takes the value one at every integration point of every segment to simplify the example. *ielem* is quadratically interpolated using the shape functions $N_{1,2,3}$ with their distributions given in the plot. The integration of each integration point value (given by blue, red and green crosses for each segment separately) is done using the shape functions of the finite element. Note that 5 integration points per segment are used. The integration using the proposed scheme gives the integrated values at the nodes of the finite element given below the plot. The obtained values at the nodes coincide with an analytical integration.

306 based on Hypoplasticity with intergranular strain extension (see (Wolffersorff, 1996) and (Niemunis and
 307 Herle, 1997)) or the advanced elasto-plastic Sanisand model (Dafalias and Manzari, 2004) are used in
 308 combination with the segment-based mortar contact discretisation. The formulation of these interface
 309 models has been presented by the authors in detail in (Staubach et al., 2022c) and has yet only been
 310 employed in conjunction with the element-based mortar contact discretisation. The general framework of
 311 the proposed interface models is shortly recapped in the following.

312 For the application of constitutive continuum models to the mechanical modelling of interfaces, the
 313 effective stress tensor and the strain tensor in the interface have to be defined. Working in the local
 314 coordinate system of the interface, only the effective normal contact stress t'_N and the two shear stress
 315 components are known. The other two (in-plane) normal stress components (see stress components $\sigma_{p1}^{\text{extra}}$
 316 and $\sigma_{p2}^{\text{extra}}$ in Fig. 4c)) are in general unknown and have to be defined.

317 The first approaches to use hypoplastic continuum models for the modelling of interfaces have been
 318 presented by (Herle and Nübel, 1999), (Gutjahr, 2003) and (Arnold and Herle, 2006; Arnold, 2008). These
 319 models are either restricted to plane conditions (Herle & Nübel, Gutjahr) or require the assumption of
 320 identical normal stress components in the interface (Arnold & Herle). The approach by Arnold & Herle
 321 has been enhanced by Stutz et al. (Stutz et al., 2016; Stutz and Mašín, 2017; Stutz et al., 2017; Stutz
 322 and Wuttke, 2018) to consider strain in the normal direction of the interface and to allow for non-
 323 identical developing normal stress components (but still identical in-plane normal stress components) in
 324 the interface element. However, the stress components still have to be set isotropic initially, contradicting
 325 typical K_0 initial stress conditions. In addition, the in-plane normal stress components in the interface are
 326 not directly governed by the boundary conditions. For instance, external loading, e.g. a traction parallel
 327 to the interface zone, can not be directly taken into account in the interface, resulting in jumps between

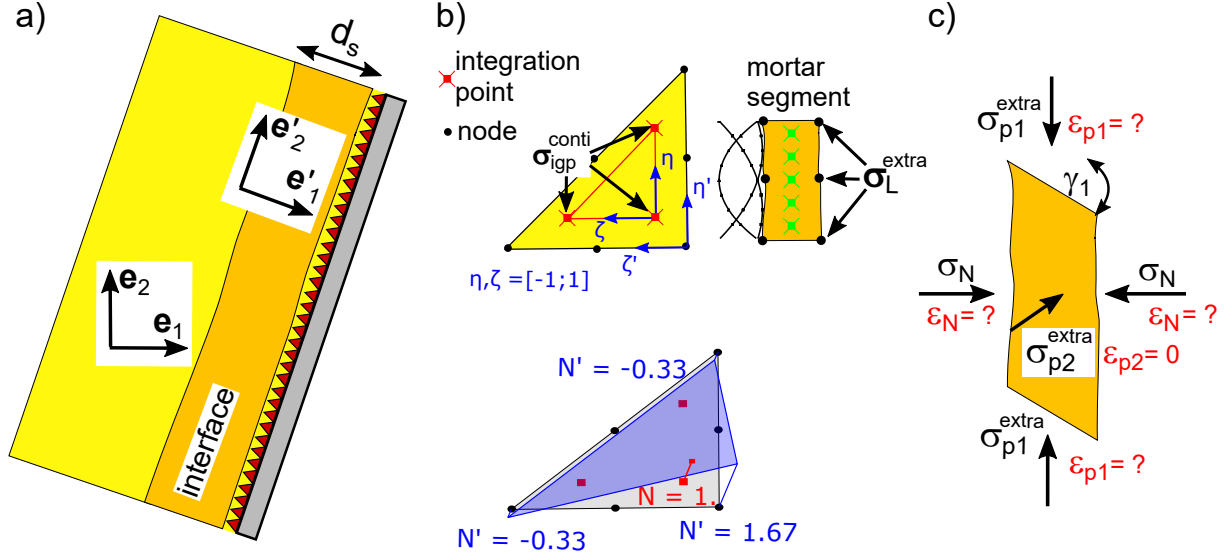


Figure 4: a) Global and local coordinate system of the interface. b) Extrapolation of the continuum stress to the interface. c) Boundary conditions and stress/strain components of the interface formulation

328 the stress components in the interface and the stress components of the adjacent continuum element. In
 329 addition, the in-plane strain components are not accounted for in the interface zone. In the approach
 330 used in this work, these shortcomings are circumvented, as is explained in the following. For the proposed
 331 interface formulation, the effective stress of the adjacent continuum is used to obtain the unknown normal
 332 stress components in the interface. The effective stress is extrapolated from the integration points of the
 333 adjacent finite element using

$$\sigma_L^{extra} = \sum_{igp}^{ngp} N_{igp}(\xi'_L, \eta'_L) \sigma_{igp}^{conti}, \quad (26)$$

334 where ξ'_L and η'_L are the stretched local coordinates of the adjacent finite element from which the effective
 335 stress is retrieved. σ_L^{extra} is the extrapolated effective stress tensor given in the global coordinate system at
 336 point L of the segment and σ_{igp}^{conti} the effective stress tensor at the integration point igp of the continuum
 337 element. Following the extrapolation, the stress has to be rotated according to the local coordinate
 338 system of the interface element given by the orthogonal unit vectors \mathbf{e}'_i , as is displayed in Fig. 4a). The
 339 extrapolation of the continuum stress to the mortar segment is schematically shown in Fig. 4b). The
 340 stress and strain conditions in the interface are depicted in Fig. 4c). Note that the stress components
 341 σ_{p1}^{extra} and σ_{p2}^{extra} are referred to as in-plane stress components (while σ_N is denoted as the out-of-plane
 342 stress component) since the general case of an interface plane in 3D space is considered. Since the normal
 343 stress components are prescribed, the normal strain of the interface has to be calculated. The strain
 344 is calculated by enforcing the internal normal stress components of the interface to be identical to the
 345 stress obtained from the continuum. The procedures performed are described in detail in (Staubach et
 346 al., 2022c). Note that, as already mentioned earlier, a zero-thickness interface formulation is adopted.
 347 However, in order to determine the shear strain for the advanced constitutive interface formulations, an
 348 interface thickness d_s has to be introduced (see Fig. 4a)). Therefore, the interface zone has a 'virtual'
 349 thickness, used to calculate the shear strain for the advanced interface formulations. Appropriate values
 350 for d_s can be determined based on the grain size of the soil and the roughness of the soil-structure
 351 interface, as is further discussed in Section 3.1.

352 Eq. (26) extrapolates the stress to the borders of the segment. Following the rotation, the values at the

353 integration points of the segments are obtained by

$$\sigma'_{\text{igp}} = \sum_L^{\text{nnode}} N_L^{\text{seg}}(\eta_{\text{igp}}) \sigma'_L{}^{\text{extra}}. \quad (27)$$

354 Alternatively, in order to avoid the additional interpolations, Eq. (26) may directly be evaluated at
355 the stretched local coordinates of the integrations points of the segment instead of the stretched local
356 coordinates of the segment borders.

357 In addition to the aforementioned considerations, the constitutive equations of the hypoplastic model
358 and the Sanisand model have to be slightly modified, accounting for the surface roughness of the soil-
359 structure interface. These modifications of the constitutive equations are described in (Staubach et al.,
360 2022c).

361 2.7 Hertzian contact problem

362 In order to evaluate the performance of the segment-based mortar method for a simple boundary value
363 problem (BVP) as well as to validate the implementation, the Hertzian contact problem is studied. In
364 addition to the segment-based method, the element-based mortar method implemented in `numgeo` is
365 considered. The adopted element-based mortar method is described in detail by the authors in (Staubach
366 et al., 2022c). Note that no additional integration points are generated at the element edges using the
367 element-based mortar method for the simulations presented in this section.

368 Figure 5 shows the adopted mesh and the material properties (Young's modulus E and Poisson's ratio
369 ν) of the deformable bodies. Only quadratically interpolated finite elements (serendipity formulation) are
370 used³. The upper sphere (radius $R = 8$ m) is loaded by an uniform vertical traction which is equivalent
371 to a force of $F = 10$ kN when integrated over the diameter. An irregular meshing with reciprocal non-
372 aligned surface nodes is used in order to better identify the differences between the contact discretisation
373 techniques. The lower sphere (radius $R = 8$ m) has exactly two times larger element edges at the surface
374 in the symmetry axis compared to the upper sphere.

375 Figure 5 displays the distribution of normal contact stress t_N with respect to the horizontal coordinate
376 starting from the symmetry axis of the model for the analytical solution based on the Hertzian contact
377 theory (see (Johnson, 1987; Popov, 2009)) and simulations using the mortar methods implemented in
378 `numgeo`.

379 Both implemented contact discretisation techniques give results which are in good accordance with the
380 results of the analytical solution. At the nodes which are close to come into contact, small deviations be-
381 tween the analytical solution and the element-based mortar method implemented in `numgeo` are observed.
382 These deviations are reduced using the segment-based mortar method due to the local refinement.

383 Overall, the differences between the two contact discretisation techniques implemented in `numgeo` are
384 small for the Hertzian contact problem. In order to investigate this for a more complex BVP, the simulation
385 of vibratory pile driving in water-saturated soil is presented in the next section.

386 3 Simulation of vibratory pile driving model tests

387 3.1 Specifications of the model tests

388 The small-scale model tests used for the back-analysis were performed by Vogelsang and are documented
389 in (Vogelsang et al., 2015; Vogelsang et al., 2017; Vogelsang, 2016). The tests are only briefly described
390 in the following since the authors have already presented simulations of the tests in previous work.

³The integration of surfaces of serendipity elements is troublesome for 3D brick elements (Buczowski et al., 1994; Buczowski, 1998; Staubach et al., 2022a). For 2D serendipity elements, however, standard interpolation functions are used to integrate the line surfaces for which no error in integration occurs.

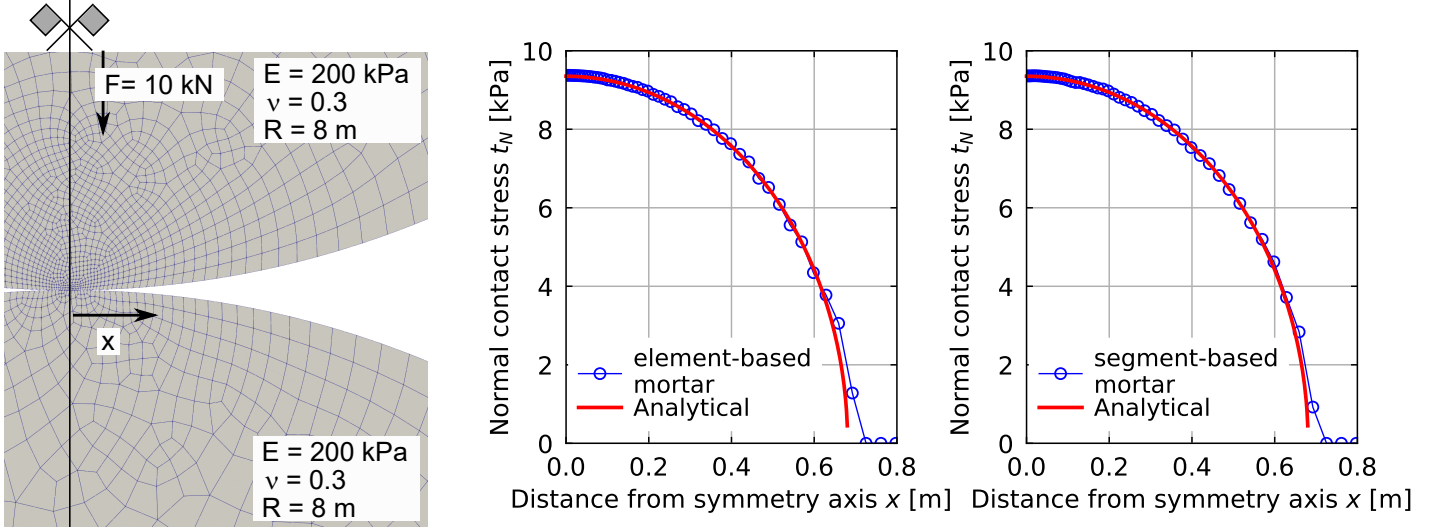


Figure 5: Model of the Hertzian contact problem (left) and normal contact stress vs. the horizontal coordinate starting from the symmetry axis of the model for the analytical solution based on the Hertzian contact theory and the simulations using the element-based and segment-based mortar methods implemented in *numgeo* (right)

391 The interested reader is referred to (Chrisopoulos and Vogelsang, 2019; Staubach and Machaček, 2019;
 392 Staubach et al., 2021b; Machaček et al., 2021b; Machaček et al., 2021a).

393 A schematic sketch and a picture of the half-axisymmetric test device are supplied in Fig. 6. The vibrator
 394 was realised as a pair of unbalances mounted on top of the pile. To measure driving forces, a load cell
 395 was placed between the vibrator and the pile. "Karlsruhe Sand" has been used as soil material, which
 396 was pluviated into deaerated water and further densified through hammer blows against the container.
 397 The final relative density was 71 % which corresponds to a porosity of $n = 0.39$ and a total density of
 398 $\rho^{tot} = 2.02 \text{ g/cm}^3$.

399 A closed-profile pile with a 60° pointed tip with a diameter of $d^{Pile} = 33 \text{ mm}$ was used in the experi-
 400 ments. The closed-profile was preferred over an open-profile in order to be able to simulate the experiments
 401 without mesh distortion using a fully Lagrangian analysis. The aluminium pile had a smooth surface and
 402 a wall friction angle of approximately $\delta \approx 1/3\varphi_c = 11^\circ$, with φ_c being the critical friction angle of the
 403 sand. Prior to driving, the pile was pushed into the sand up to a depth of approximately 15 cm. During
 404 driving, the vibrator was free to move in vertical direction and its self-weight of 6594 g was completely
 405 carried by the pile. After 6.35 s of vibration with a frequency of 25 Hz, the rotating unbalances were
 406 stopped but the measuring continued for a short time.

407 3.2 Numerical model

408 The mesh adopted for the simulations including boundary conditions and dimensions is given in Fig. 6c.
 409 A zoom on the pile tip is shown in Fig. 13, which is discussed later. Both the geometry of the pile and the
 410 geometry of the soil are discretised with quadratically interpolated finite elements. A full axisymmetric
 411 model is used. The forces and masses are scaled to fit to the half-axisymmetric experimental set-up. The
 412 so-called zipper-method is used to avoid mesh distortion when the pile penetrates into the soil (Berg, 1994;
 413 Henke, S., Grabe, J., 2008). The load cell is replaced by a spring with identical stiffness. The driving force
 414 of the vibrator is applied on this spring and transferred to the top of the pile. A geometrically non-linear
 415 calculation is performed and the Zaremba-Jaumann stress rate integrated employing the Hughes-Winget
 416 algorithm (Hughes and Winget, 1980) is used (updated Lagrangian analysis (Belytschko et al., 2001)).
 417 The \mathbf{u} - p formulation spatially discretising the balance of linear momentum of the mixture and the mass
 418 balance of the pore water is applied. The spatially discretised balance equations are given in Appendix
 419 A. It is well known that the \mathbf{u} - p formulation neglects the relative acceleration between the solid and the

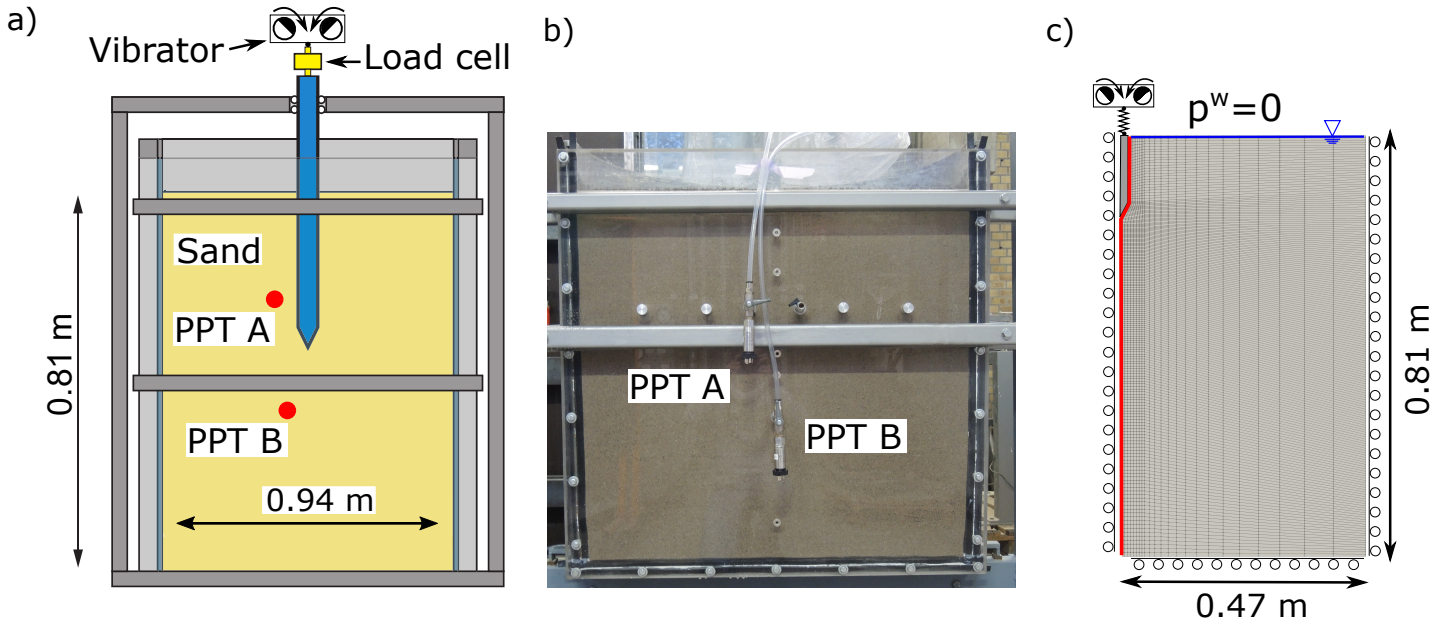


Figure 6: a) Schematic drawing of the front of the test device with location of pore pressure transducers (PPT). b) Photo of the device (based on (Vogelsang et al., 2015; Vogelsang et al., 2017)). c) Finite element model for the Lagrangian simulation. The red line in Fig. c) indicates the extension of the pile used for the zipper-method.

420 water phase, which can be of importance for high wave frequencies in soil with high hydraulic conductivity.
 421 In a preceding study, the authors demonstrated that the relative acceleration can be neglected for the
 422 vibratory pile driving process based on simulations using \mathbf{u} - p - \mathbf{U} and \mathbf{u} - \mathbf{U} finite element formulations
 423 which account for relative acceleration (Staubach and Machaček, 2019). Hence, the \mathbf{u} - p formulation is
 424 judged to be appropriate. The Hilber-Hughes-Taylor (Hilber et al., 1977) time integration scheme with
 425 a constant time increment of $\Delta t = 0.001$ s and a value of $\alpha = -0.05$ for the numerical damping is used
 426 during the dynamic part of the simulation.

427 The bulk modulus of the pore water is assumed to be $\bar{K}^w = 1.1 \cdot 10^4$ kPa (corresponding to a degree of
 428 saturation of $S \approx 99.9\%$) accounting for minor air inclusion originating from the sand pluviation process.
 429 The Kozeny/Carman equation (Kozeny Josef, 1927; Carman, 1939) is used to account for the influence of
 430 the porosity n on the hydraulic conductivity. This is judged important due to the large volumetric strain
 431 occurring during the pile driving process leading to a considerable change in hydraulic conductivity in
 432 vicinity of the pile. The required parameters have been derived experimentally by Vogelsang and are given
 433 in (Vogelsang et al., 2017; Machaček et al., 2021b). The spatial distribution of the hydraulic conductivity
 434 during the pile driving process is given in Appendix C. Due to the loosening of the soil close to the pile,
 435 considerably larger values of hydraulic conductivity are obtained in the vicinity of the pile compared to
 436 the initial values. However, lower values are obtained in greater distance to the pile. The consideration
 437 of the change in hydraulic conductivity due to a change in porosity leads to higher pile penetration rates
 438 compared to constant values, which is also demonstrated in Appendix C. No drainage is possible normal
 439 to the pile-soil interface, which is realised by not prescribing the pore water pressure at the surface nodes
 440 of the soil. It is known that such interfaces are preferred flow paths for the pore water, which can be
 441 taken into account using hydro-mechanically coupled interface elements (see e.g. (Segura and Carol, 2008;
 442 Cerfontaine et al., 2015; Cui et al., 2019)). For instance, these formulations allow for a storage of water
 443 in the interface zone, which is only indirectly possible to account for using the approach applied in this
 444 work. The increased water content at the soil-pile interface during the uplift phase is a result of the
 445 no-separation condition in the present approach, leading to high expansion of the soil and thereby an
 446 increase in the porosity (i.e. the water content). Since the Kozeny/Carman equation is used, the higher
 447 hydraulic conductivity is taken into account in this zone. A transport of pore water normal through the

interface (i.e. transversal flow), possible to account for by some of the mentioned interface models, is however not relevant for the simulations presented here, since the pile does not allow for the adsorption of water.

For both the continuum and the interface the hypoplastic model with intergranular strain extension is used as constitutive model. The constitutive parameters for "Karlsruhe Sand" have been derived from an extensive laboratory testing program documented in (Machaček et al., 2021b). The parameters are given in Table 1. In addition, simulations using the Sanisand interface formulation are performed. The parameters of Sanisand have also been calibrated for "Karlsruhe Sand" in (Machaček et al., 2021b) and are supplied in Table 2. For the advanced interface models, two additional parameters are necessary, which are the surface roughness κ , given by $\kappa = \tan(\delta)/\tan(\varphi_c) = 0.3$ and the interface thickness estimated as $d_s = 5$ mm, which corresponds to $\approx 10 \cdot d_{50}$. This is a value for the interface thickness frequently observed in experiments (Hu and Pu, 2004; DeJong et al., 2006; DeJong and Westgate, 2009; Martinez et al., 2015). d_{50} is the median grain size of "Karlsruhe Sand". If the Coulomb interface model is used for comparison purpose, the only parameters required are the wall friction angle δ and the tangential stiffness (estimated to 3000 kPa).

φ_c	h_s	n	e_{d0}	e_{c0}	e_{i0}	α	β	m_T	m_R	R	β_R	χ
33.1°	19 GPa	0.285	0.549	0.851	0.979	0.1	0.32	1.2	2.4	$5 \cdot 10^{-5}$	0.08	7

Table 1: Parameters of the hypoplastic model with intergranular strain extension for "Karlsruhe Sand" (Machaček et al., 2021b)

p_a	e_0	λ_c	ξ	M_c	c	m	G_0
100 kPa	1.1	0.25	0.35	1.3	0.88	0.05	70
ν	h_0	c_h	n_b	A_0	n_d	z_{\max}	c_z
0.05	8	0.35	1.3	0.8	0.8	60	2000

Table 2: Parameters of the Sanisand model for "Karlsruhe Sand" (Machaček et al., 2021b)

Due to the strongly non-linear distribution of contact stress during the vibratory pile driving process, an exact integration of contact stress is of great importance. The mortar segments are integrated using five integration points for the following simulation. Compared to the element-based mortar technique a much more refined surface discretisation is therefore applied (at least twice as many integration points using the segment-based mortar method with more integration points closer to the pile tip). Additional simulations with the element-based technique using five integration points is performed in order to evaluate the two different techniques for comparable numbers of integration points.

3.3 Results of the simulations

For the evaluation of the pile penetration the normalised pile displacement \tilde{u}_y is used, which is defined by

$$\tilde{u}_y = \frac{u_y}{d_{Pile}}. \quad (28)$$

In Eq. (28), u_y is the vertical displacement of the pile. The normalised pile displacement \tilde{u}_y vs. time of vibration for the simulations using the two mortar techniques and the different interface models is given in Fig. 7. Note that for the experiment only the mean trend of pile penetration is depicted. Given the complexity of the BVP, the simulations reproduce the measured values well and the difference between the simulations is relatively small. The element-based mortar method using the Coulomb interface model predicts the lowest pile penetration rate while the segment-based mortar method in combination with the

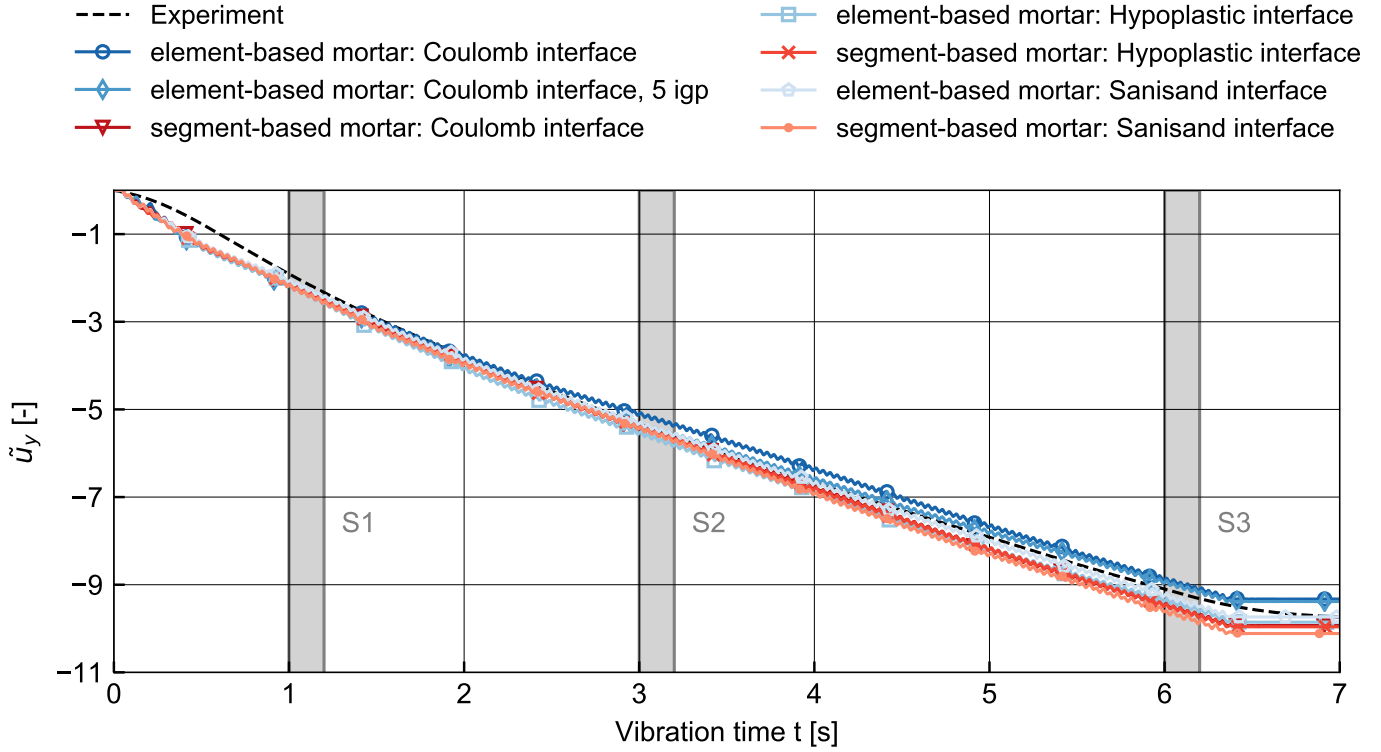


Figure 7: Comparison of normalised pile displacement \tilde{u}_y vs. time of vibration for the measured values and the simulations using the element-based and the segment-based mortar contact discretisation technique in combination with the different interface models. In addition, one simulation using the element-based technique with five integration points per finite element edge instead of three is given.

477 Sanisand interface model shows the highest pile penetration rate. In general, the segment-based mortar
 478 method gives higher pile penetration rates than the element-based method. The simulation employing the
 479 element-based mortar method in conjunction with the Coulomb friction model and five integration points
 480 also shows a higher penetration rate in comparison to the corresponding simulation with three integration
 481 points for the first 4 s of driving. However, towards the end of the simulation, the two simulations reach
 482 almost identical values of \tilde{u}_y . At the beginning of the driving process ($t \approx 0.2$ s), the element-based mortar
 483 method with the Coulomb interface model shows an irregular pattern of displacement amplitudes, which
 484 is absent in the results using the segment-based mortar method with the Coulomb friction model. Towards
 485 the end of the driving process both mortar methods incorporating the Sanisand interface model show
 486 irregular patterns of \tilde{u}_y as well, with every second cycle showing a lower amplitude.

487 In order to better visualise the mentioned irregularities, the evolution of the normalised pile displace-
 488 ment is given in detail for the time frames *S1*, *S2* and *S3* (marked in Fig. 7) in Fig. 8, showing the results
 489 for all utilised interface models. For the time frames *S1* and *S2* all simulations show a harmonic sinusoidal
 490 pile displacement with almost constant amplitudes, whereas for time frame *S3* both mortar methods in
 491 combination with the Sanisand interface model show noticeable irregularities, with every second cycle
 492 showing a smaller amplitude. For both mortar techniques the Sanisand interface model shows a higher
 493 pile penetration at time frame *S3* compared to the simulations with the Coulomb interface model. Using
 494 the hypoplastic interface model, the results almost coincide with the results of the Coulomb interface
 495 model in case of the segment-based method but higher penetration rates for the element-based mortar
 496 method are observed.

497 Compared to the results of the experiment, all simulations predict too large amplitudes of displacement.
 498 This deviation has also been observed for earlier simulations of the vibratory pile driving tests reported
 499 in (Chrisopoulos and Vogelsang, 2019) and its further investigation is not subject of the present work.

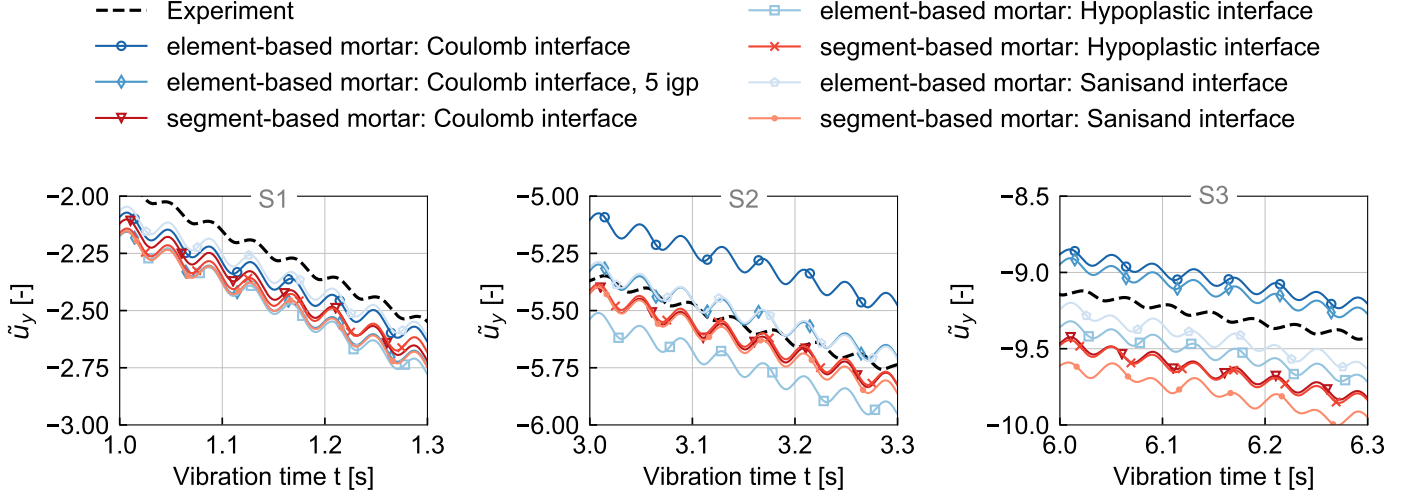


Figure 8: Normalised pile displacement \tilde{u}_y vs. time of vibration for the time frames $S1$, $S2$ and $S3$ marked in Fig. 7 for the measured values and the simulations using the element-based and the segment-based mortar contact discretisation technique in combination with different interface models

To further analyse the differences between the mortar methods, the pile force measured between vibrator and pile head is evaluated. Note that this force is not identical to the prescribed force at the mass point connected to the spring due to inertia forces. The normalised pile force is defined by

$$\tilde{F}^{Pile} = \frac{F^{Pile}}{F_{stat}^{Pile}}, \quad (29)$$

500 where F_{stat}^{Pile} is the static pile force resulting from the dead weight of the pile, the oscillator and the load
501 cell. In the simulations, the pile force results from the integration of the contact stresses along the paired
502 surfaces and is therefore strongly influenced by the contact discretisation technique. The normalised pile
503 displacement \tilde{u}_y vs. normalised pile force is given for the experiment and the simulations using the different
504 mortar techniques with the Coulomb and the Sanisand interface model in Fig. 9 for the time frame $S2$
505 and in Fig. 10 for the time frame $S3$. For all simulations the accordance of the results with the measured
506 values is acceptable but the magnitude of normalised pile force is underestimated. The potential reason
507 for this deviation is most likely the set of parameters of the hypoplastic model used for the modelling
508 of the continuum. Simulations using a different parameter set for "Karlsruhe Sand" reported and used
509 for the simulation of the vibratory pile driving tests in (Chrisopoulos and Vogelsang, 2019) result in a
510 much better representation of the pile driving force. However, much too low excess pore water pressures
511 are predicted using this (to some extent randomly chosen) parameter set. In addition, this parameter set
512 does not reproduce results of undrained cyclic triaxial tests on "Karlsruhe Sand" well. The comparison
513 of the measured excess pore water pressures with the values obtained by the present simulations is given
514 in Fig. 15 of the appendix.

515 Compared to the element-based mortar method, the segment-based technique gives a more regular
516 course of \tilde{F}^{Pile} for both interface models. The better performance of the segment-based mortar method
517 can be traced back to the finer surface discretisation, leading to a smoother distribution of contact stress
518 and a more precise integration (to prove this, a simulation using the element-based approach with more
519 integration points is discussed later). The magnitude of minimum and maximum forces predicted by the
520 two mortar methods is comparable, however. In addition, the differences between the interface models are
521 found to be almost negligible for time frame $S2$. This is not unexpected since for smooth soil-structure
522 interfaces such as is the case for the aluminium pile utilised in the experiment, the constitutive interface
523 behaviour is very similar to shearing of an initially loose soil sample (i.e. no peak in the τ - γ plot prior
524 to the critical state and almost no dilatancy/constant dilatancy angle). These characteristics can be

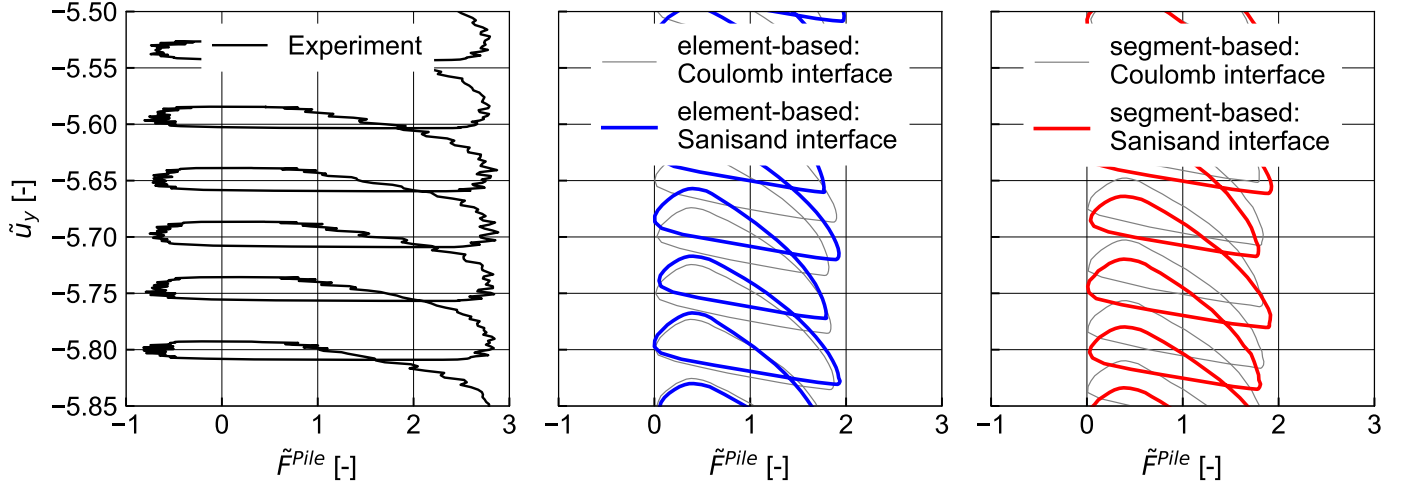


Figure 9: Normalised pile displacement \tilde{u}_y vs. normalised pile force \tilde{F}^{Pile} during time frame $S2$ (marked in Fig. 7) for the values measured in the experiment and the simulations using the element-based and the segment-based mortar contact discretisation technique in combination with the Coulomb and the Sanisand interface model, respectively

525 described well by the Coulomb model. In addition, due to the increase in pore water pressure caused by
 526 the vibration of the pile, the effective stress in the vicinity of the pile shaft is significantly reduced, limiting
 527 the maximum frictional stresses that can be mobilised and thus the overall influence of the friction model.

528
 529 As has been observed in Figs. 7 and 8, the differences between the two mortar techniques in terms of
 530 pile penetration increase with increasing time of vibration. In line with this, the differences in terms of
 531 force between vibrator and pile also increase accordingly, as is visible from Fig. 10 displaying the results
 532 for time frame $S3$. Due to the lower displacement amplitude in every second cycle observed in Fig. 8,
 533 the \tilde{u}_y vs. \tilde{F}^{Pile} plot obtained using the element-based mortar method shows a much smaller amplitude
 534 of normalised pile force for every second cycle, being more pronounced in case of the Sanisand interface
 535 model. In contrast, a more regular course is obtained using the segment-based technique for both interface
 536 models. The results of the segment-based technique are also in better accordance with the experimental
 537 results, since they show a regular course of force as well. However, a tiny irregularity within the first
 538 visible cycle is encountered using the segment-based mortar technique. This can (at least partially) be
 539 explained by the distortion of the finite elements close to the pile shoulder as is shown and discussed later
 540 for Fig. 13.

541 Figure 11 depicts the \tilde{u}_y vs. \tilde{F}^{Pile} plot for the time frame $S3$ using the two discretisation techniques
 542 with the Coulomb and the hypoplastic interface model, respectively. Compared to the Sanisand interface
 543 model, for both contact discretisation techniques a more regular development of \tilde{F}^{Pile} is observed. The
 544 differences between the two mortar methods are also much less pronounced compared to the simulations
 545 using the Sanisand interface model.

546 In order to assess the influence of the number of integration points used for the element-based mortar
 547 discretisation, the normalised pile displacement \tilde{u}_y vs. normalised pile force \tilde{F}^{Pile} during time frame
 548 $S3$ is compared for simulations using the Coulomb and the Sanisand interface models with three and
 549 five integration points per element edge in Fig. 12. Note that in contrast to the segment-based mortar
 550 technique, the total number of integration points stays constant throughout the simulation since the
 551 number of elements at the surface pair does not change. Note in addition that for most states during the
 552 driving process, the simulation with the element-based technique and five integration points per element
 553 surface still results in a lower total number of integration points of the surface pair, since for the seg-
 554 ment-based method much more points are generated at the pile surface, having much larger elements than the
 555 soil surface (see Fig. 13). The comparison of the simulations with different numbers of integration points

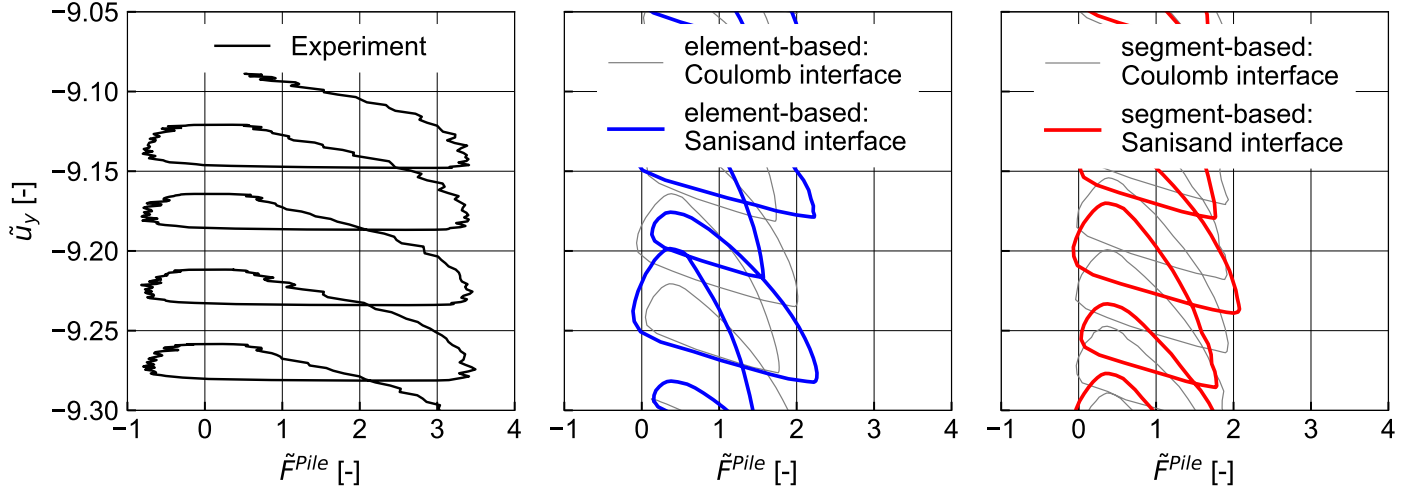


Figure 10: Normalised pile displacement \tilde{u}_y vs. normalised pile force \tilde{F}^{Pile} during time frame $S3$ (marked in Fig. 7) for the values measured in the experiment and the simulations using the element-based and the segment-based mortar contact discretisation technique in combination with the Coulomb and the Sanisand interface model, respectively

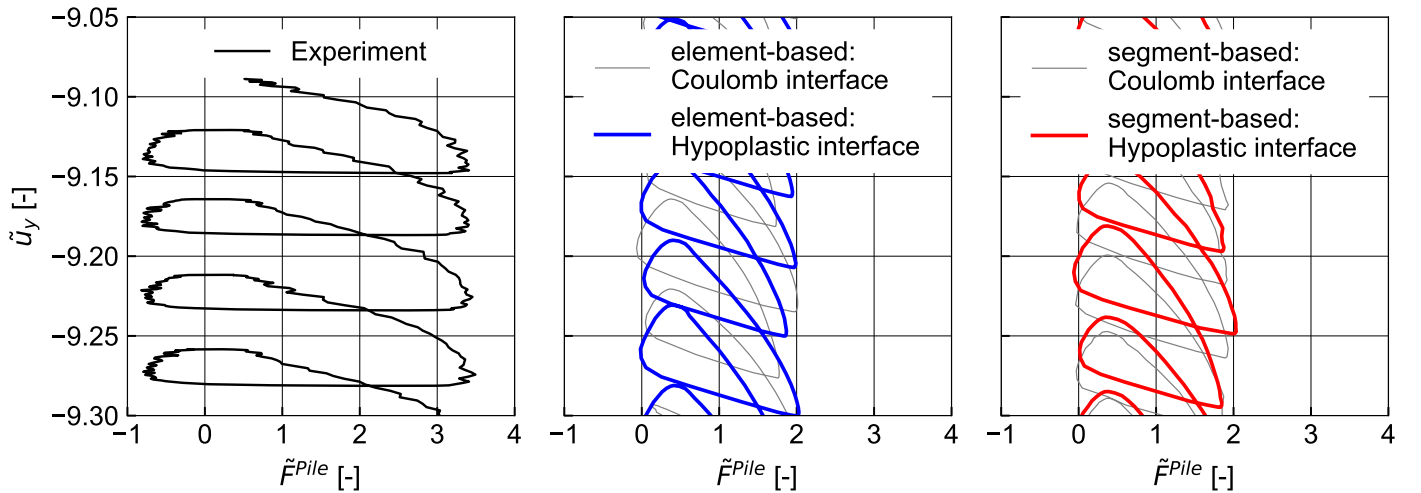


Figure 11: Normalised pile displacement \tilde{u}_y vs. normalised pile force \tilde{F}^{Pile} during time frame $S3$ (marked in Fig. 7) for the values measured in the experiment and the simulations using the element-based and the segment-based mortar contact discretisation technique in combination with the Coulomb and the hypoplastic interface model, respectively

556 shows that the influence is rather small for the Coulomb interface model, but quite large for the Sanisand
 557 interface model. Using five integration points instead of three results in a more regular development of
 558 \tilde{F}^{Pile} and less differences in the maximum values between subsequent cycles. However, some irregularities
 559 within individual cycles are visible. As has been mentioned earlier, they are believed to be (at least
 560 partially) caused by the distortion of the finite elements close to the pile shoulder as is discussed later on
 561 the basis of Fig. 13.

562 Overall, the results for the element-based method with five integration points are similar to those
 563 for the corresponding simulation using the segment-based method given in Fig. 10. Hence, the better
 564 performance of the segment-based method mentioned earlier can partly be traced back to the larger
 565 number of integration points and not to the method itself.

566 The left-hand side of Fig. 13 displays the spatial distribution of the effective horizontal stress acting in

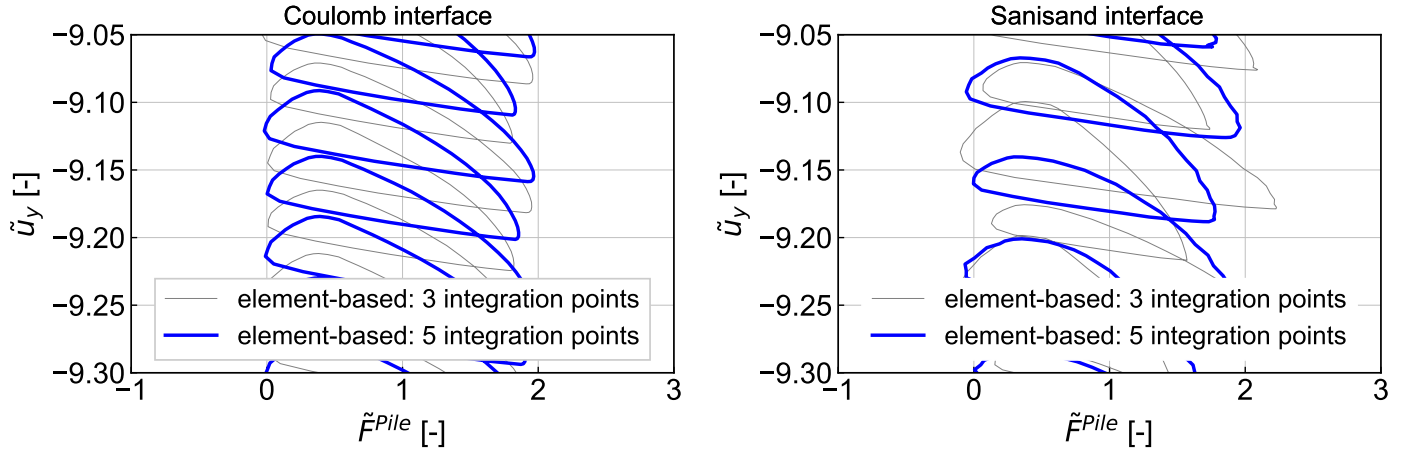


Figure 12: Normalised pile displacement \tilde{u}_y vs. normalised pile force \tilde{F}^{Pile} during time frame $S3$ (marked in Fig. 7) for the simulations using the element-based mortar contact discretisation technique in combination with the Coulomb and the Sanisand interface model and different number of integration points of the mortar contact

567 the vicinity of the pile tip for the two mortar contact discretisation techniques using the Coulomb friction
568 model at a time of vibration of 1.31 s (end of time frame $S1$). The deformed configuration without a
569 deformation scale factor is given. A distortion of the elements close to the pile shoulder is visible, which
570 is believed to cause some of the aforementioned irregularities in the predicted forces (see e.g. Fig. 12 and
571 Fig. 10). This could be remedied by employing re-meshing algorithms or large-deformation techniques
572 (e.g. ALE algorithms). However, these numerical schemes add complexity and potentially additional
573 numerical problems, for why "only" an updated Lagrangian scheme is used in the present work. High
574 values of effective horizontal stress are observed at the pile shoulder for both contact discretisation
575 techniques. Considering the small dimensions of the model tests, these values are judged to be quite
576 high, representing stress conditions which would also be expected in case of much larger piles (e.g. several
577 decimetres in diameter). The plots on the right-hand side of Fig. 13 depict the effective horizontal, effective
578 vertical and shear stress along the pile surface with respect to the vertical coordinate (starting from the
579 bottom of the soil container) for the two different mortar techniques. The element-based technique shows
580 slightly higher values and less regular distributions of the stress components, the latter in particular for
581 the distribution of shear stress. The higher stresses visible for the element-based technique also agree well
582 with the lower pile penetration rate observed in Fig. 7 and Fig. 8 compared to the segments-based mortar
583 technique. Overall, however, the differences rather small.

584 Table 3 gives the number of iterations and the time spent in the contact routines for the different
585 simulations. Note that all simulations are performed using four native cores and the same clock-speed.
586 The number of required iterations is similar for the simulations using the Coulomb interface models.
587 This is because during the dynamic pile driving process, convergence is achieved within the first iteration
588 for almost all increments. In contrast, the time spent in the contact routines, including all procedures
589 involving contacts (contact search, contact discretisation, calculation and integration of contact stress,
590 assembling of contact forces), depends on the mortar method and the interface model adopted. Note
591 that nearly all time-consuming processes of both mortar methods are performed with multiple threads.
592 However, the parallelisation is slightly more efficient for the segment-based mortar approach, since the
593 same strategies for parallelisation as used for regular finite elements can be applied, reducing overhead
594 compared to the element-based approach. Unsurprisingly, for the Coulomb interface model the segment-
595 based mortar method takes approximately 1.5 times longer than the element-based mortar method using 3
596 integration points per finite element edge, which is due to the larger number of surface points at which the
597 contact stress is evaluated and integrated. In addition, the evaluation of the segments has to be performed,
598 which is not necessary with the element-based mortar method. Compared to the total simulation time
599 (approximately 27000 s), however, the differences in time required for the contact routines are almost

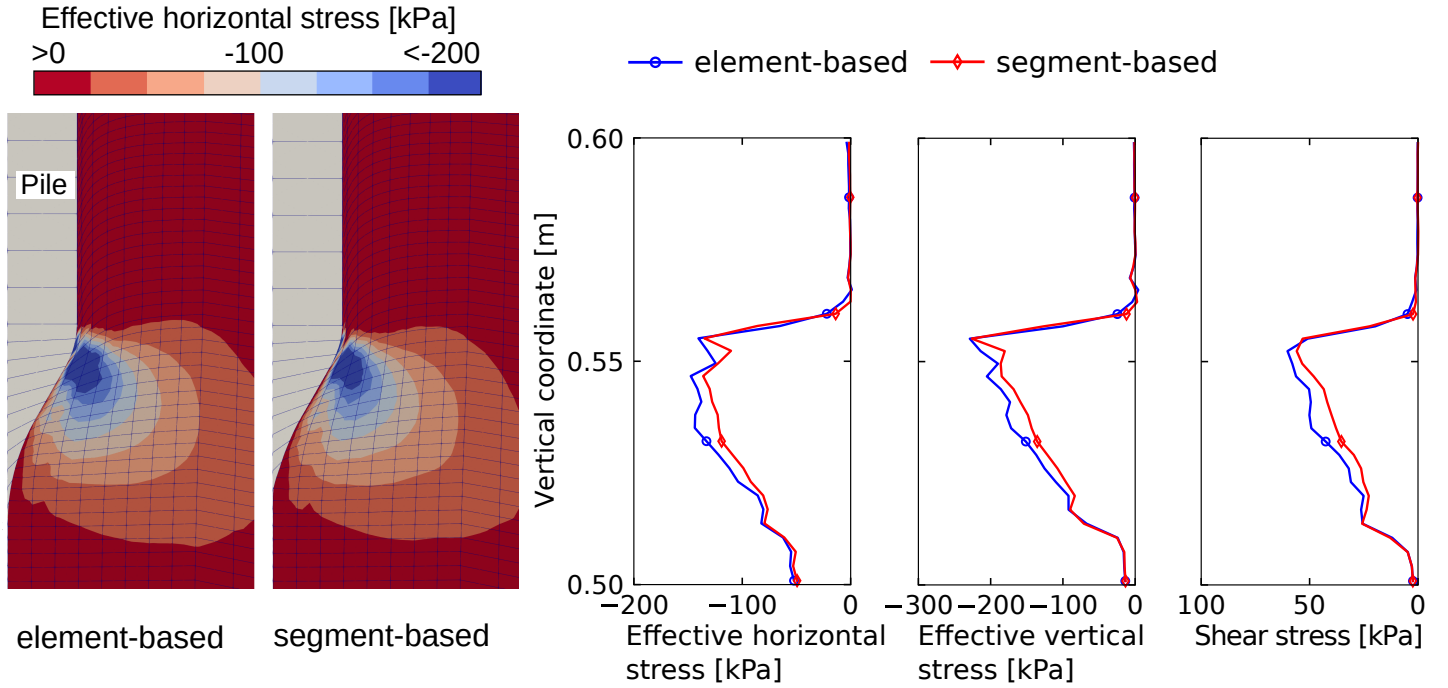


Figure 13: Spatial distributions of effective horizontal stress acting in the vicinity of the pile tip at a time of vibration of 1.31 s (end of time frame *S1*) for the simulations using the element-based and the segment-based mortar contact discretisation with the Coulomb friction model. In addition, the distributions of effective horizontal, effective vertical and shear stresses with respect to the vertical coordinate, starting from the bottom of the container, are given along the pile surface for the two mortar techniques.

negligible. Using five integration points per finite element edge for the element-based technique results in more time spent in the contact routine compared to the segment-based approach using the same number of integration points per segment.

The simulation using the hypoplastic interface model requires more time for the contact routines compared to the Coulomb interface model, for both mortar techniques. In addition, a slightly larger number of iterations is required in case of the element-based approach. Similar to the differences observed for the Coulomb interface model, the segment-based mortar method takes approximately 1.5 times longer than the element-based mortar method due to the larger number of integration points. However, compared to the total time of the simulation (slightly larger than 27000 s for both simulations), these differences are judged insignificant. In contrast, using the Sanisand interface model results in far more iterations and longer times spent in the contact routines, in particular for the element-based approach. This fits well to the course of force depicted in Fig. 10, for which strong irregularities are observed using the element-based approach.

4 Conclusions

A segment-based mortar contact discretisation technique for the analysis of problems with large deformations allowing to utilise sophisticated constitutive interface models has been presented and its performance has been compared to a simpler element-based mortar method. Both contact discretisation techniques are implemented in the finite element code `numgeo`.

The following conclusions are drawn:

- The implementation of a segment-based mortar method is more complex and more prone to errors than an element-based technique. However, a multi-threaded implementation is more straightforward for the segment-based mortar method, since the same strategies as used for the assembling of finite elements can be applied.

Simulation	No. of iterations	Time contact [s]
Element-based: Coulomb interface	7016	277
Element-based (5 igp): Coulomb interface	7017	499
Segment-based: Coulomb interface	7017	450
Element-based: Hypoplastic interface	7080	416
Segment-based: Hypoplastic interface	7015	610
Element-based: Sanisand interface	9115	1568
Segment-based: Sanisand interface	7677	1355

Table 3: Number of iterations and (physical) time spent in the contact routines for the different simulations. The time spent in the (continuum) element loop is approximately 16000 s and the time needed to solve the system-of-equations approximately 10000 s for the simulations using the Coulomb interface model. The total time is approximately 27000 s for the simulations using the Coulomb interface model. The contact routines, element loop and the solver are all run with four native cores (one Intel®Core™ i9 9900K processor with four cores run with the base-frequency of 3.6 GHz without utilising Hyper-threading is used).

- 623 • For simple BVPs such as the Hertzian contact problem both mortar methods were found to perform
624 comparably.
- 625 • For the analysis of vibratory pile driving, the segment-based mortar contact discretisation proved to
626 be more robust in terms of numerical stability compared to the element-based mortar method. This
627 was especially evident with respect to the predicted force between the vibrator and the pile head
628 in the simulations using the Sanisand interface model, for which the element-based mortar method
629 showed stronger irregularities, which were absent when applying the segment-based technique. The
630 results using the segment-based mortar method were observed to be in better agreement with
631 the measured forces. However, using the element-based mortar method with a larger number of
632 integration points per finite element edge resulted in less irregularities, giving pile forces similar to
633 the segment-based approach.
- 634 • Following these conclusions, it is apparent that the contact discretisation technique plays a key role
635 in obtaining numerically stable results for the analysis of pile installation processes.
- 636 • In terms of computational performance, the segment-based mortar contact discretisation was found
637 to be comparable to the element-based method, if a comparable number of integration points was
638 used.
- 639 • The comparison of simulations using a hypoplastic and a Sanisand interface model with simulations
640 using a simple Coulomb friction model showed that the constitutive interface model influenced the
641 pile penetration during the vibratory driving comparatively little. In terms of force between the
642 vibrator and the pile head, almost no influence from the constitutive interface model was found.
643 When interpreting these conclusions, it must be taken into account that the pile surface was smooth.
- 644 • The numerical stability is only moderately influenced by the constitutive interface model despite the
645 much more complex and strongly non-linear response of the hypoplastic interface model compared
646 to the Coulomb friction model. However, using the Sanisand interface formulation, more iterations
647 were required and much more time was spent in the contact routines.

648 Future work will investigate the influence of the constitutive interface models for the simulation of vi-
649 bratory pile driving with rough soil-pile interfaces. A much larger influence of the constitutive interface
650 models is expected compared to the simulations presented in this work.

651 Acknowledgements

652 The authors are grateful to Jakob Vogelsang for providing the experimental data.

653 Author contribution statement

654 Patrick Staubach: Writing - original draft, Conceptualisation, Software, Formal analysis, Data curation,
655 Visualisation, Validation

656 Jan Machaček: Software, Writing - review & editing

657 Torsten Wichtmann: Funding acquisition, Writing - review & editing

658 A Spatially discretised balance equations

659 For the spatial discretisation of the continuum, the finite element method in an updated Lagrangian
660 framework is used. The global coordinate $\mathbf{x}(\boldsymbol{\xi})$ at the local finite element coordinate $\boldsymbol{\xi}$ is calculated by

$$\mathbf{x}(\boldsymbol{\xi}) = \sum_I N_I(\boldsymbol{\xi}) \mathbf{x}_I, \quad (30)$$

661 where the interpolation function $N_I(\boldsymbol{\xi})$ is one at node I for the functions used in the present work. \mathbf{x}_I is
662 the global coordinate of node I .

663 The so-called element *Jacobian* \mathbf{J} is the derivative of the global coordinates with respect to the local
664 coordinates and given by

$$\mathbf{x}_{,\xi}(\boldsymbol{\xi}) = \sum_I \frac{dN_I(\boldsymbol{\xi})}{d\xi} \mathbf{x}_I. \quad (31)$$

665 Using Eq. (31), the normal vector $\mathbf{n}(\xi)$ at the edge of a finite element interpolated with the local coordinate
666 ξ is given for 2D or axisymmetric cases by

$$\mathbf{n}(\xi) = \frac{\mathbf{x}_{,\xi}(\xi) \times \boldsymbol{\tau}_3}{\|\mathbf{x}_{,\xi}(\xi)\|}, \quad (32)$$

667 where $\boldsymbol{\tau}_3$ is the in-plane unit vector and \times marks the cross product. The tangential vector of the element
668 edge is determined using

$$\boldsymbol{\tau}(\xi) = \frac{\mathbf{x}_{,\xi}(\xi)}{\|\mathbf{x}_{,\xi}(\xi)\|}. \quad (33)$$

669 The spatially discretised balance equations for the continuum are given in the following. The soil is
670 understood as a two-phase medium consisting of solid grains (s) and pore water (w). The volume fraction
671 concept of the *Theory of Porous Media* (TPM) is used to describe the mixture (see e.g. (Schrefler et al.,
672 1990; Ehlers and Bluhm, 2013)). In the framework of the TPM, the heterogeneous body is decomposed into
673 homogeneous sub-bodies, forming a statistical surrogate model. The partial densities are $\rho^s = (1 - n)\bar{\rho}^s$
674 and $\rho^w = n\bar{\rho}^w$, where $n = 1 - \varphi^s = \varphi^w$ is the porosity, φ^s is the volume fraction of the solid phase and
675 φ^w is the volume fraction of the water phase. Intrinsic values are written as $\bar{\square}$ with $\bar{\rho}^s$ and $\bar{\rho}^w$ being the
676 intrinsic densities of the solid and water phase, respectively.

677 For the \mathbf{u} - p formulation, the degrees of freedom (*dofs*), namely the displacement of the solid \mathbf{u} and

678 the pore water pressure p^w , are interpolated using the interpolation functions N_J and \hat{N}_K , i.e.

$$679 \quad \mathbf{u} = \sum_J N_J \mathbf{u}_J \quad \text{and} \quad p^w = \sum_K \hat{N}_K p_K^w. \quad (34)$$

680 To satisfy the Ladyshenskaya-Babuška-Brezzi condition (Falk, 1993), the solid displacement is interpo-
681 lated using quadratic shape functions N_J while the pore water pressure is interpolated using linear shape
682 functions \hat{N}_K (Taylor and Hood, 1973).

683 Considering the contributions of the contact constraints given by Eq. (21), the discretised form of the
684 balance equation of linear momentum of the mixture is defined by

$$685 \quad \begin{aligned} \mathbf{r}_I^s = & \int_{\Omega} \text{grad}(N_I) \cdot \boldsymbol{\sigma} d\Omega - \int_{\Omega} \text{grad}(N_I) \cdot \mathbf{I} \hat{N}_K p_K^w d\Omega - \int_{\Gamma^C} \mathbf{t}_I^C d\Gamma^C \\ & - \int_{\Gamma} \hat{\mathbf{t}}_I d\Gamma - \int_{\Omega} N_I \rho^{tot} \mathbf{b} d\Omega + \int_{\Omega} N_I [(1-n)\bar{\rho}^s + n\bar{\rho}^w] N_J \ddot{\mathbf{u}}_J d\Omega \stackrel{!}{=} \mathbf{0}, \end{aligned} \quad (35)$$

686 where $\boldsymbol{\sigma}$ is the effective stress tensor, \mathbf{t}_I^C is the (total) contact traction and $\hat{\mathbf{t}}_J$ are the external total
687 tractions acting on the boundary Γ . \mathbf{I} is the unit tensor and \mathbf{b} a body force. ρ^{tot} is the total density. \mathbf{r}_I^s
688 corresponds to the residuum of the balance equation of linear momentum and is minimised iteratively
689 using the Newton-Raphson scheme.

690 The spatially discretised balance of mass of the pore water reads

$$691 \quad \begin{aligned} r_K^p = & \int_{\Omega} \hat{N}_K \frac{n}{\bar{K}^w} \hat{N}_L \dot{p}_L^w d\Omega + \int_{\Gamma} q^w \hat{N}_K d\Gamma + \int_{\Omega} \hat{N}_K \frac{1}{\bar{K}^w} \text{grad}(\hat{N}_L) \cdot \mathbf{w}^w p_L^w d\Omega \\ & + \int_{\Omega} \text{grad}(\hat{N}_K) \cdot (\bar{\rho}^w k^w \mathbf{I} \cdot N_J \ddot{\mathbf{u}}_J) d\Omega + \int_{\Omega} k^w \text{grad}(\hat{N}_K) \cdot \mathbf{I} \cdot \text{grad}(\hat{N}_L) p_L^w d\Omega \\ & - \int_{\Omega} k^w \text{grad}(\hat{N}_K) \cdot \mathbf{I} \cdot \mathbf{b} \bar{\rho}^w d\Omega + \int_{\Omega} \hat{N}_K \text{grad}(N_J) \cdot \dot{\mathbf{u}}_J^s d\Omega \stackrel{!}{=} 0, \end{aligned} \quad (36)$$

692 where q^w is a prescribed flow of pore water. To calculate the relative velocity \mathbf{w}^w between the solid
693 skeleton and pore water, the generalised Darcy law is used, which is given by

$$694 \quad \mathbf{w}^w = \frac{\mathbf{K}^w}{\bar{\rho}^w \|\mathbf{b}\|} \cdot \left[-\text{grad}(p^w) + \bar{\rho}^w (\mathbf{b} - \ddot{\mathbf{u}}) \right], \quad (37)$$

695 where $\mathbf{K}^w(n)$ is the hydraulic conductivity tensor (assumed isotropic in the present case $\mathbf{K}^w = \mathbf{I}k^w$).
696 Using the Kozeny/Carman equation, $\mathbf{K}^w(n)$ is a function of the porosity n .

697 **B Derivatives of contact contributions for the segment-based** 698 **mortar contact discretisation**

699 For the Newton-Raphson algorithm the derivatives of the balance equations given in Appendix A with
700 respect to the solid displacement \mathbf{u} and the pore water pressure p^w are required. The analytical calculation
701 of the derivatives of the contact contributions using the segment-based mortar method is presented in
702 the following. The derivatives of the other contributions not connected to contacts can be found e.g. in
703 (Li et al., 2004).

704 First, the derivatives of the normal vector (Section B.1), the local convective coordinates and integration
705 area (Sections B.2, B.3 and Section B.4) and the normal contact stress (Section B.5) are calculated.
706 Following, the complete contributions are presented in Section B.6 for the normal contact stress and in
707 Section B.7 for the tangential contact stress.

704 B.1 Derivatives of the normal vector

705 Recalling the definition of the normal vector introduced in Eq. (32) and introducing the non-normalised
706 normal vector $\hat{\mathbf{n}}(\xi_{\text{igp}})$

$$\mathbf{n}(\xi_{\text{igp}}) = \frac{\sum_I^{\text{nnode}} \frac{\partial N_I(\xi_{\text{igp}})}{\partial \xi} \mathbf{x}_I \times \boldsymbol{\tau}_3}{\left\| \sum_I^{\text{nnode}} \frac{\partial N_I(\xi_{\text{igp}})}{\partial \xi} \mathbf{x}_I \right\|} = [\hat{\mathbf{n}}(\xi_{\text{igp}})]^{\rightarrow} \quad (38)$$

707 the derivative with respect to the displacement is defined by

$$\frac{\partial \mathbf{n}(\xi_{\text{igp}})}{\partial \mathbf{u}_J} = \frac{\frac{\partial \hat{\mathbf{n}}(\xi_{\text{igp}})}{\partial \mathbf{u}_J}}{\|\hat{\mathbf{n}}(\xi_{\text{igp}})\|} - \frac{\left[\hat{\mathbf{n}}(\xi_{\text{igp}}) \cdot \frac{\partial \hat{\mathbf{n}}(\xi_{\text{igp}})}{\partial \mathbf{u}_J} \right] \hat{\mathbf{n}}(\xi_{\text{igp}})}{\|\hat{\mathbf{n}}(\xi_{\text{igp}})\|^3}. \quad (39)$$

708 In Eq. (39), the differential Δ of the norm of a vector \sqcup defined by

$$\Delta \|\sqcup\| = \frac{\sqcup \cdot \Delta \sqcup}{\|\sqcup\|} \quad (40)$$

709 is used. $\frac{\partial \hat{\mathbf{n}}(\xi_{\text{igp}})}{\partial \mathbf{u}_J}$ is given by

$$\frac{\partial \hat{\mathbf{n}}(\xi_{\text{igp}})}{\partial \mathbf{u}_J} = \frac{\partial}{\partial \mathbf{u}_J} \left[\sum_I^{\text{nnode}} \frac{\partial N_I(\xi_{\text{igp}})}{\partial \xi} \mathbf{x}_I \times \boldsymbol{\tau}_3 \right] = -\frac{\partial N_J(\xi_{\text{igp}})}{\partial \xi} \text{skew}(\boldsymbol{\tau}_3), \quad (41)$$

710 where $\text{skew}(\sqcup)$ is defined by

$$[\text{skew}(\sqcup)] = \begin{bmatrix} 0 & -\sqcup_3 & \sqcup_2 \\ \sqcup_3 & 0 & -\sqcup_1 \\ -\sqcup_2 & \sqcup_1 & 0 \end{bmatrix}. \quad (42)$$

711 In a similar way the derivatives of the tangential vector is obtained.

712 B.2 Derivatives of the convective coordinate

713 The goal is to derive an explicit expression for the derivative of the convective coordinate $\bar{\xi}^{(2)}$ with
714 respect to the displacement of node I . The term used for the calculation of the convective coordinate
715 $\mathbf{g}_I \cdot \mathbf{x}_{,\xi}^{(2)}(\bar{\xi}^{(2)}) = \left[\sum_J^{\text{nnode}} N_J^{(2)}(\bar{\xi}^{(2)}) \mathbf{x}_J^{(2)} - \mathbf{x}_I^{(1)} \right] \cdot \mathbf{x}_{,\xi}^{(2)}(\bar{\xi}^{(2)})$ can be differentiated with respect to $\mathbf{u}_I^{(1)}$ yielding

$$\frac{\partial}{\partial \mathbf{u}_I^{(1)}} \left\{ \left[\sum_J^{\text{nnode}} N_J^{(2)}(\bar{\xi}^{(2)}) \mathbf{x}_J^{(2)} - \mathbf{x}_I^{(1)} \right] \cdot \mathbf{x}_{,\xi}^{(2)}(\bar{\xi}^{(2)}) \right\} = \mathbf{0}. \quad (43)$$

716 Using the chain-rule, the following expression is obtained

$$\begin{aligned} & \left[\sum_J^{\text{nnode}} \frac{\partial}{\partial \bar{\xi}^{(2)}} N_J^{(2)}(\bar{\xi}^{(2)}) \mathbf{x}_J^{(2)} \frac{\partial \bar{\xi}^{(2)}}{\partial \mathbf{u}_I^{(1)}} + \sum_J^{\text{nnode}} N_J^{(2)}(\bar{\xi}^{(2)}) \frac{\partial \mathbf{x}_J^{(2)}}{\partial \mathbf{u}_I^{(1)}} - \frac{\partial \mathbf{x}_I^{(1)}}{\partial \mathbf{u}_I^{(1)}} \right] \cdot \sum_J^{\text{nnode}} N_{J,\xi}^{(2)}(\bar{\xi}^{(2)}) \mathbf{x}_J^{(2)} \\ & + \mathbf{g}_I \cdot \sum_J^{\text{nnode}} \frac{\partial}{\partial \bar{\xi}^{(2)}} N_{J,\xi}^{(2)}(\bar{\xi}^{(2)}) \frac{\partial \bar{\xi}^{(2)}}{\partial \mathbf{u}_I^{(1)}} \mathbf{x}_J^{(2)} + \mathbf{g}_I \cdot \sum_J^{\text{nnode}} N_{J,\xi}^{(2)}(\bar{\xi}^{(2)}) \frac{\partial \mathbf{x}_J^{(2)}}{\partial \mathbf{u}_I^{(1)}} = \mathbf{0}. \end{aligned} \quad (44)$$

717 Simplifying and rearranging yields

$$\begin{aligned}
& \left[\sum_J^{\text{nnode}} N_{J,\xi}^{(2)}(\bar{\xi}^{(2)}) \mathbf{x}_J^{(2)} \cdot \sum_J^{\text{nnode}} N_{J,\xi}^{(2)}(\bar{\xi}^{(2)}) \mathbf{x}_J^{(2)} + \mathbf{g}_I \cdot \sum_J^{\text{nnode}} N_{J,\xi\xi}^{(2)}(\bar{\xi}^{(2)}) \mathbf{x}_J^{(2)} \right] \frac{\partial \bar{\xi}^{(2)}}{\partial \mathbf{u}_I^{(1)}} \\
& + \sum_J^{\text{nnode}} N_J^{(2)}(\bar{\xi}^{(2)}) \frac{\partial \mathbf{x}_J^{(2)}}{\partial \mathbf{u}_I^{(1)}} \cdot \sum_J^{\text{nnode}} N_{J,\xi}^{(2)}(\bar{\xi}^{(2)}) \mathbf{x}_J^{(2)} - \sum_J^{\text{nnode}} N_{J,\xi}^{(2)}(\bar{\xi}^{(2)}) \mathbf{x}_J^{(2)} \\
& + \mathbf{g}_I \cdot \sum_J^{\text{nnode}} N_{J,\xi}^{(2)}(\bar{\xi}^{(2)}) \frac{\partial \mathbf{x}_J^{(2)}}{\partial \mathbf{u}_I^{(1)}} = \mathbf{0}.
\end{aligned} \tag{45}$$

718 Solving for $\frac{\partial \bar{\xi}^{(2)}}{\partial \mathbf{u}_I^{(1)}}$ and considering that $\frac{\partial \mathbf{x}_J^{(2)}}{\partial \mathbf{u}_I^{(1)}} = \mathbf{0}$ holds results in

$$\frac{\partial \bar{\xi}^{(2)}}{\partial \mathbf{u}_I^{(1)}} = - \frac{- \sum_J^{\text{nnode}} N_{J,\xi}^{(2)}(\bar{\xi}^{(2)}) \mathbf{x}_J^{(2)}}{\sum_J^{\text{nnode}} N_{J,\xi}^{(2)}(\bar{\xi}^{(2)}) \mathbf{x}_J^{(2)} \cdot \sum_J^{\text{nnode}} N_{J,\xi}^{(2)}(\bar{\xi}^{(2)}) \mathbf{x}_J^{(2)} + \mathbf{g}_I \cdot \sum_J^{\text{nnode}} N_{J,\xi\xi}^{(2)}(\bar{\xi}^{(2)}) \mathbf{x}_J^{(2)}}. \tag{46}$$

719 Proceeding analogously but differentiating with respect to $\mathbf{u}_J^{(2)}$ gives

$$\frac{\partial \bar{\xi}^{(2)}}{\partial \mathbf{u}_J^{(2)}} = - \frac{N_J^{(2)}(\bar{\xi}^{(2)}) \sum_J^{\text{nnode}} N_{J,\xi}^{(2)}(\bar{\xi}^{(2)}) \mathbf{x}_J^{(2)} + \mathbf{g}_I N_{J,\xi}^{(2)}(\bar{\xi}^{(2)})}{\sum_J^{\text{nnode}} N_{J,\xi}^{(2)}(\bar{\xi}^{(2)}) \mathbf{x}_J^{(2)} \cdot \sum_J^{\text{nnode}} N_{J,\xi}^{(2)}(\bar{\xi}^{(2)}) \mathbf{x}_J^{(2)} + \mathbf{g}_I \cdot \sum_J^{\text{nnode}} N_{J,\xi\xi}^{(2)}(\bar{\xi}^{(2)}) \mathbf{x}_J^{(2)}}. \tag{47}$$

720 The derivatives of $\bar{\xi}^{(1)}$ are obtained analogously.

721 B.3 Derivatives of local segment coordinates

722 For the segment-based mortar contact discretisation, the derivatives of the local coordinates of the seg-
723 ment are required. The derivative of the local coordinate of the finite element given in terms of the
724 local coordinate of the segment calculated using Eq. (13) with respect to the nodal displacement for
725 quadratically interpolated finite elements is given by

$$\frac{\partial \xi^{(i)}(\eta)}{\partial \mathbf{u}_I^{(i)}} = -\frac{1}{2}\eta(1-\eta) \frac{\partial \xi_a^{(i)}}{\partial \mathbf{u}_I^{(i)}} + \frac{1}{2}\eta(1+\eta) \frac{\partial \xi_b^{(i)}}{\partial \mathbf{u}_I^{(i)}} + (1-\eta^2) \frac{\partial \xi_c^{(i)}}{\partial \mathbf{u}_I^{(i)}}. \tag{48}$$

726 The derivatives of the local convective coordinates at the segment borders ($\xi_a^{(i)}$ and $\xi_b^{(i)}$) can be obtained
727 with the formulas that have been derived in the previous Section. The derivative of the local coordinate
728 at the mid of the segment $\xi_c^{(i)}$ can directly be calculated using

$$\frac{\partial \xi_c^{(i)}}{\partial \mathbf{u}_I^{(i)}} = \left(\frac{\partial \xi_a^{(i)}}{\partial \mathbf{u}_I^{(i)}} + \frac{\partial \xi_b^{(i)}}{\partial \mathbf{u}_I^{(i)}} \right) / 2. \tag{49}$$

729 B.4 Derivatives of the integration area

730 The derivative of $j_{\text{igp}}^{(i)} = \left\| \frac{\partial \mathbf{x}^{(i)}(\xi_{\text{igp}})}{\partial \xi^{(i)}} \right\| \frac{\partial \xi^{(i)}(\eta_{\text{igp}})}{\partial \eta}$ depends on the interpolation order of the finite elements.

731 For quadratically interpolated elements, the second term of $j_{\text{igp}}^{(i)}$ is

$$\frac{\partial \xi^{(i)}(\eta_{\text{igp}})}{\partial \eta} = -\frac{1}{2}(1 - \eta_{\text{igp}})\xi_a^{(i)} + \frac{1}{2}\eta_{\text{igp}}\xi_a^{(i)} + \frac{1}{2}(1 + \eta_{\text{igp}})\xi_b^{(i)} + \frac{1}{2}\eta_{\text{igp}}\xi_b^{(i)} + (1 - 2\eta_{\text{igp}})\xi_c^{(i)} \quad (50)$$

732 and the derivative with respect to the displacement consequently given by

$$\begin{aligned} \frac{\partial \xi^{(i)}(\eta_{\text{igp}})}{\partial \mathbf{u}_I^{(i)} \partial \eta} &= -\frac{1}{2}(1 - \eta_{\text{igp}}) \frac{\partial \xi_a^{(i)}}{\partial \mathbf{u}_I^{(i)}} + \frac{1}{2}\eta_{\text{igp}} \frac{\partial \xi_a^{(i)}}{\partial \mathbf{u}_I^{(i)}} + \frac{1}{2}(1 + \eta_{\text{igp}}) \frac{\partial \xi_b^{(i)}}{\partial \mathbf{u}_I^{(i)}} \\ &+ \frac{1}{2}\eta_{\text{igp}} \frac{\partial \xi_b^{(i)}}{\partial \mathbf{u}_I^{(i)}} + (1 - 2\eta_{\text{igp}}) \frac{\partial \xi_c^{(i)}}{\partial \mathbf{u}_I^{(i)}}. \end{aligned} \quad (51)$$

733 Recalling Eq. (40), the first term of Eq. (50) for quadratically or higher order interpolated elements is
734 defined by

$$\frac{\partial}{\partial \mathbf{u}_I^{(i)}} \left\| \frac{\partial \mathbf{x}^{(i)}(\xi_{\text{igp}})}{\partial \xi^{(i)}} \right\| = \frac{\partial \mathbf{x}^{(i)}(\xi_{\text{igp}})}{\partial \xi^{(i)}} \frac{\partial}{\partial \mathbf{u}_I^{(i)}} \frac{\partial \mathbf{x}^{(i)}(\xi_{\text{igp}})}{\partial \xi^{(i)}} / \left\| \frac{\partial \mathbf{x}^{(i)}(\xi_{\text{igp}})}{\partial \xi^{(i)}} \right\|. \quad (52)$$

735 B.5 Normal contact contributions and derivative of the normal contact 736 stress

737 Assuming a frictionless case using the penalty regularisation ($t_{N,\text{igp}} = \varepsilon g_{N,\text{igp}}$, $\mathbf{t}_{T,\text{igp}}^{(i)} = \mathbf{0}$), the contact
738 contribution given by Eq. (22) to the balance of linear momentum is rewritten to

$$\mathbf{r}_{N,I}^{(i)} = \sum_{\text{igp}}^{\text{ngp}} N_I^{(i)}(\xi^{(i)}(\eta_{\text{igp}})) t_{N,\text{igp}} \mathbf{n}_{\text{igp}}^{(i)} w_{\text{igp}} j_{\text{igp}}^{(i)}. \quad (53)$$

739 Note that the scalar normal contact stress is identical for both surfaces i , hence allowing to drop the
740 exponent. Using the penalty regularisation, the normal contact stress is calculated by multiplying the
741 normal gap $g_{N,\text{igp}}$ defined by Eq. (18) with the penalty factor ε yielding

$$\begin{aligned} t_{N,\text{igp}} &= \varepsilon g_{N,\text{igp}} = \varepsilon (\mathbf{x}_{\text{igp}}^{(2)} - \mathbf{x}_{\text{igp}}^{(1)}) \cdot \mathbf{n}_{\text{igp}}^{(1)} \\ &= \varepsilon \left\{ \sum_I^{\text{nnode}} N_I(\xi^{(2)}(\eta_{\text{igp}})) \mathbf{x}_I^{(2)} - \sum_J^{\text{nnode}} N_J(\xi^{(1)}(\eta_{\text{igp}})) \mathbf{x}_J^{(1)} \right\} \cdot \mathbf{n}_{\text{igp}}^{(1)}. \end{aligned} \quad (54)$$

742 The derivative of the normal contact stress $t_{N,\text{igp}}$ with respect to the corresponding displacement $\mathbf{u}_J^{(i)}$
743 for $i = 1$ is

$$\begin{aligned} \frac{\partial t_{N,\text{igp}}}{\partial \mathbf{u}_J^{(1)}} &= -\varepsilon N_J(\xi^{(1)}(\eta_{\text{igp}})) \mathbf{n}_{\text{igp}}^{(1)} + \varepsilon (\mathbf{x}_{\text{igp}}^{(2)} - \mathbf{x}_{\text{igp}}^{(1)}) \cdot \frac{\partial \mathbf{n}_{\text{igp}}^{(1)}}{\partial \mathbf{u}_J^{(1)}} \\ &+ \varepsilon \left\{ \sum_I^{\text{nnode}} N_{I,\xi}(\xi^{(2)}(\eta_{\text{igp}})) \frac{\partial \xi^{(2)}}{\partial \mathbf{u}_J^{(1)}} \otimes \mathbf{x}_I^{(2)} - \sum_J^{\text{nnode}} N_{J,\xi}(\xi^{(1)}(\eta_{\text{igp}})) \frac{\partial \xi^{(1)}}{\partial \mathbf{u}_J^{(1)}} \otimes \mathbf{x}_J^{(1)} \right\} \cdot \mathbf{n}_{\text{igp}}^{(1)} \end{aligned} \quad (55)$$

744 and for $i = 2$

$$\begin{aligned} \frac{\partial t_{N,\text{igp}}}{\partial \mathbf{u}_I^{(2)}} &= \varepsilon N_I[\xi^{(2)}(\eta_{\text{igp}})] \mathbf{n}_{\text{igp}}^{(1)} + \varepsilon (\mathbf{x}_{\text{igp}}^{(2)} - \mathbf{x}_{\text{igp}}^{(1)}) \cdot \frac{\partial \mathbf{n}_{\text{igp}}^{(1)}}{\partial \mathbf{u}_I^{(2)}} \\ &+ \varepsilon \left\{ \sum_I^{\text{nnode}} N_{I,\xi}(\xi^{(2)}(\eta_{\text{igp}})) \frac{\partial \xi^{(2)}}{\partial \mathbf{u}_J^{(2)}} \otimes \mathbf{x}_I^{(2)} - \sum_J^{\text{nnode}} N_{J,\xi}(\xi^{(1)}(\eta_{\text{igp}})) \frac{\partial \xi^{(1)}}{\partial \mathbf{u}_J^{(2)}} \otimes \mathbf{x}_J^{(1)} \right\} \cdot \mathbf{n}_{\text{igp}}^{(1)}. \end{aligned} \quad (56)$$

745 The required derivatives of the local finite element coordinates depending on the local segment coordinate
746 and of the normal vector have already been derived previously. From the terms given in Eqs. (55, 56),
747 the first is the most decisive.

748 B.6 Derivatives of the normal contact contributions

749 Using Eqs. (39, 50, 51, 55), the normal contact contribution of node I of the slave surface with respect to
750 the displacement of a node I at the slave surface using the segment-based mortar contact discretisation
751 is given by

$$\begin{aligned} \frac{\partial \mathbf{r}_{N,I}^{(1)}}{\partial \mathbf{u}_I^{(1)}} &= \sum_{\text{igp}}^{\text{ngp}} \left\{ N_I^{(1)}(\xi^{(1)}(\eta_{\text{igp}})) \frac{\partial t_{N,\text{igp}}}{\partial \mathbf{u}_I^{(1)}} \otimes \mathbf{n}_{\text{igp}}^{(1)} w_{\text{igp}} j_{\text{igp}}^{(1)} + N_{I,\xi}^{(1)}(\xi^{(1)}(\eta_{\text{igp}})) \frac{\partial \xi^{(1)}(\eta_{\text{igp}})}{\partial \mathbf{u}_I^{(1)}} t_{N,\text{igp}} \mathbf{n}_{\text{igp}}^{(1)} w_{\text{igp}} j_{\text{igp}}^{(1)} \right. \\ &+ N_I^{(1)}(\xi^{(1)}(\eta_{\text{igp}})) t_{N,\text{igp}} \frac{\partial \mathbf{n}_{\text{igp}}^{(1)}}{\partial \mathbf{u}_I^{(1)}} w_{\text{igp}} j_{\text{igp}}^{(1)} + N_I^{(1)}(\xi^{(1)}(\eta_{\text{igp}})) t_{N,\text{igp}} \mathbf{n}_{\text{igp}}^{(1)} w_{\text{igp}} \\ &\left. \left[\frac{\partial \mathbf{x}^{(1)}(\xi_{\text{igp}})}{\partial \xi^{(1)}} \frac{\partial \partial \mathbf{x}^{(1)}(\xi_{\text{igp}})}{\partial \mathbf{u}_I^{(1)} \partial \xi^{(1)}} \frac{\partial \xi^{(1)}(\eta_{\text{igp}})}{\partial \eta} \right] / \left\| \frac{\partial \mathbf{x}^{(1)}(\xi_{\text{igp}})}{\partial \xi^{(1)}} \right\| + \left\| \frac{\partial \mathbf{x}^{(1)}(\xi_{\text{igp}})}{\partial \xi^{(1)}} \right\| \frac{\partial \partial \xi^{(1)}(\eta_{\text{igp}})}{\partial \mathbf{u}_I^{(1)} \partial \eta} \right] \right\}. \end{aligned} \quad (57)$$

752 $\frac{\partial \mathbf{r}_{N,I}^{(2)}}{\partial \mathbf{u}_I^{(2)}}$ is obtained analogously. In addition, the terms $\frac{\partial \mathbf{r}_{N,I}^{(1)}}{\partial \mathbf{u}_J^{(2)}}$ and $\frac{\partial \mathbf{r}_{N,J}^{(2)}}{\partial \mathbf{u}_I^{(1)}}$ have to be accounted for, which
753 consider the change of the contact forces with respect to the displacement of the paired surface node
754 (Habracken and Cescotto, 1998). Again, the first term in Eq. (57) is the most decisive. Very conveniently,
755 the terms $\frac{\partial \mathbf{r}_{N,I}^{(1)}}{\partial \mathbf{u}_J^{(2)}}$ and $\frac{\partial \mathbf{r}_{N,J}^{(2)}}{\partial \mathbf{u}_I^{(1)}}$ are identical in magnitude to $\frac{\partial \mathbf{r}_{N,I}^{(1)}}{\partial \mathbf{u}_I^{(1)}}$ and $\frac{\partial \mathbf{r}_{N,I}^{(2)}}{\partial \mathbf{u}_I^{(2)}}$ (but have opposite sign) if
756 only the first term of Eq. (57) is considered.

757 B.7 Derivatives of the tangential contact contributions

758 The contribution to the force equilibrium of the frictional contact forces $\mathbf{r}_{T,I}^{(i)}$ is given by

$$\mathbf{r}_{T,I}^{(i)} = \sum_{\text{igp}}^{\text{ngp}} N_I^{(i)}(\xi^{(i)}(\eta_{\text{igp}})) t_{T,\text{igp}}^{(i)} \boldsymbol{\tau}_{\text{igp}}^{(i)} w_{\text{igp}} j_{\text{igp}}^{(i)} \quad \text{for } i = \{1, 2\}. \quad (58)$$

759 The tangential contact stress is a function of the tangential gap and can also be a function of the effective
760 normal contact stress $t'_{N,\text{igp}}$. The derivative with respect to the displacement is given by

$$\frac{\partial t_{T,\text{igp}}^{(i)}}{\partial \mathbf{u}_I^{(i)}} = \frac{\partial t_{T,\text{igp}}^{(i)}}{\partial t'_{N,\text{igp}}} \frac{\partial t'_{N,\text{igp}}}{\partial \mathbf{u}_I^{(i)}} + \frac{\partial t_{T,\text{igp}}^{(i)}}{\partial g_{T,\text{igp}}} \frac{\partial g_{T,\text{igp}}}{\partial \mathbf{u}_I^{(i)}} \quad \text{for } i = \{1, 2\}. \quad (59)$$

761 The derivatives $\frac{\partial t_{T,\text{igp}}^{(i)}}{\partial t'_{N,\text{igp}}}$ and $\frac{\partial t_{T,\text{igp}}^{(i)}}{\partial g_{T,\text{igp}}}$ are calculated in dependence of the friction model used. They can
 762 be found in the literature for the Coulomb friction model. If the advanced interface models are applied,
 763 a numerical differentiation is used (Staubach et al., 2022c), making the analytical calculation of the
 764 derivatives obsolete.

765 $\frac{\partial g_{T,\text{igp}}}{\partial \mathbf{u}_I^{(i)}}$ is given in analogy to Eq. (55) by

$$\begin{aligned} \frac{\partial g_{T,\text{igp}}}{\partial \mathbf{u}_I^{(1)}} = & -N_I^{(1)}(\xi^{(1)}(\eta_{\text{igp}}))\boldsymbol{\tau}_{\text{igp}}^{(1)} + (\mathbf{x}_{\text{igp}}^{(2)} - \mathbf{x}_{\text{igp}}^{(1)}) \cdot \frac{\partial \boldsymbol{\tau}_{\text{igp}}^{(1)}}{\partial \mathbf{u}_I^{(1)}} \\ & + \left\{ \sum_I^{\text{nnode}} N_{I,\xi}(\xi^{(2)}(\eta_{\text{igp}})) \frac{\partial \xi^{(2)}}{\partial \mathbf{u}_I^{(1)}} \otimes \mathbf{x}_I^{(2)} - \sum_J^{\text{nnode}} N_{J,\xi}(\xi^{(1)}(\eta_{\text{igp}})) \frac{\partial \xi^{(1)}}{\partial \mathbf{u}_I^{(1)}} \otimes \mathbf{x}_J^{(1)} \right\} \cdot \boldsymbol{\tau}_{\text{igp}}^{(1)}. \end{aligned} \quad (60)$$

766 The remaining derivatives of Eq. (58) are obtained analogously to Eq. (57).

767 Equation (58) also depends on the pore water pressure p^w since the effective normal contact stress is
 768 used for the update of the tangential stress. The derivative of the effective normal contact with respect
 769 to the pore water pressure p_K^w at node K is

$$\frac{\partial t'_{N,\text{igp}}}{\partial p_K^w} = N_K^{\text{seg}}(\eta_{\text{igp}}). \quad (61)$$

770 This defines the derivative of the tangential stress with respect to p_K^w

$$\frac{\partial t_{T,\text{igp}}^{(i)}}{\partial p_K^w} = \frac{\partial t_{T,\text{igp}}^{(i)}}{\partial t'_{N,\text{igp}}} \frac{\partial t'_{N,\text{igp}}}{\partial p_K^w}. \quad (62)$$

771 C Spatial distribution of hydraulic conductivity during driving 772 and influence of a porosity-dependent hydraulic conductivity 773 ity

774 As has been explained in Section 3.1, the Kozeny/Carman equation is used to consider the influence
 775 of the change in porosity on the hydraulic conductivity k^w . The spatial distributions of the hydraulic
 776 conductivity at 2 s and at 6.35 s of vibratory driving are given on the left-hand side of Fig. 14. It
 777 is well visible that due to the loosening of the soil close to the pile shaft the hydraulic conductivity
 778 increases approximately by a factor 2 in that zone. This creates a preferred dissipation path for excess
 779 pore water pressure in the vicinity of the pile. Due to compaction of the soil at greater distances from
 780 the pile shaft the hydraulic conductivity slightly decreases there, which leads to a large gradient of
 781 k^w with respect to the radial distance from the pile shaft. The plot on the right-hand side of Fig.
 782 14 compares the normalised pile penetration vs. vibration time from simulations using either a constant
 783 hydraulic conductivity $k^w = 1.1 \cdot 10^{-3}$ m/s (corresponding to the value obtained using the Kozeny/Carman
 784 equation with the initial value of porosity) or the Kozeny/Carman equation ($k^w(n)$). The segment-based
 785 mortar contact discretisation with Coulomb friction is applied in both cases. While for the first 3 s both
 786 simulations coincide, the simulation assuming a constant value of k^w leads to less pile penetration towards
 787 the end of the driving phase. This can be explained by the high gradient of k^w for the simulation with $k^w(n)$
 788 resulting in worse drainage conditions in radial direction in the vicinity of the pile tip. Therefore, higher
 789 excess pore water pressures develop in vicinity of the pile tip for the simulation using the Kozeny/Carman
 790 equation. This is demonstrated in Fig. 15, where the normalised excess pore water pressure $\Delta p^w/p_0^w$ at
 791 PPT B (see Fig. 6) measured in the experiment and obtained from the simulations using either a constant
 792 hydraulic conductivity k^w or the Kozeny/Carman equation ($k^w(n)$) is displayed. Δp^w denotes the change

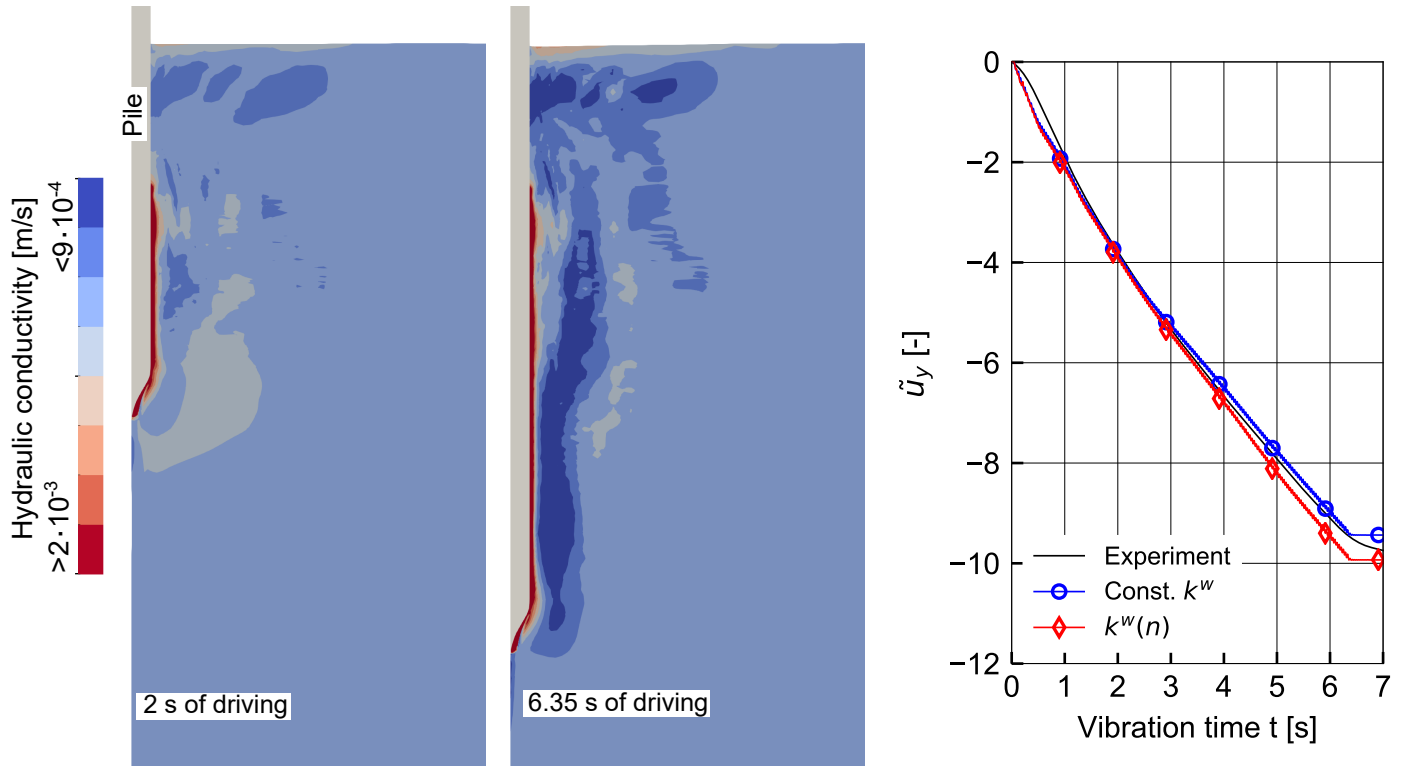


Figure 14: Spatial distribution of hydraulic conductivity at 2 s and at the end of driving (6.35 s) using the Kozeny/Carman equation (left) and normalised pile penetration vs. vibration time utilising either a constant hydraulic conductivity k^w or the Kozeny/Carman equation ($k^w(n)$) for simulations with the segment-based mortar technique and Coulomb friction (right)

793 in pore water pressure relative to the hydrostatic pore water pressure p_0^w . At the time of vibration the
 794 pile tip passes the transducer (at approximately 5.6 s for $k^w(n)$ and 5.9 s for the constant value of k^w)
 795 the simulation with $k^w(n)$ shows slightly larger values of $\Delta p^w/p_0^w$ compared to the simulation with a
 796 constant value of k^w . However, even before the pile tip reaches PPT B, the consideration of the variable
 797 hydraulic conductivity leads to larger excess pore water pressures, which also fit better to the measured
 798 values compared to the simulation with constant k^w .

799 In addition to the higher excess pore water pressure developing in case of $k^w(n)$, the shear stress that
 800 can be mobilised at the pile shaft is also lower, since the upward directed flow of pore water tangentially
 801 to the pile-soil interface close to the pile shaft reduces the effective stress in the interface zone.

802 References

- 803 El-Abbasi, N. and K. J. Bathe (June 2001). “Stability and patch test performance of contact dis-
 804 cretizations and a new solution algorithm”. In: *Computers and Structures* 79.16, pp. 1473–1486. ISSN:
 805 00457949. DOI: [10.1016/S0045-7949\(01\)00048-7](https://doi.org/10.1016/S0045-7949(01)00048-7).
- 806 Arnold, M. (2008). *Application of the intergranular strain concept to the hypoplastic modelling of non-*
 807 *adhesive interfaces*. Vol. 1. Conference IACMAG, 1-6 October, Goa-India, pp. 747–754. ISBN: 9781622761760.
- 808 Arnold, M. and I. Herle (2006). “Hypoplastic description of the frictional behaviour of contacts”. In:
 809 *Proceedings of the 6th European Conference on Numerical Methods in Geotechnical Engineering - Nu-*
 810 *merical Methods in Geotechnical Engineering*. Ed. by H. Schweiger, pp. 101–106. ISBN: 0415408229.
 811 DOI: [10.1201/9781439833766.ch14](https://doi.org/10.1201/9781439833766.ch14).
- 812 Belytschko, T., W. K. Liu, B. Moran, and K. Elkhodary (2001). *Nonlinear finite elements for continua*
 813 *and structures*. Vol. 38. 07. John wiley & sons, pp. 38–3926–38–3926. DOI: [10.5860/choice.38-3926](https://doi.org/10.5860/choice.38-3926).

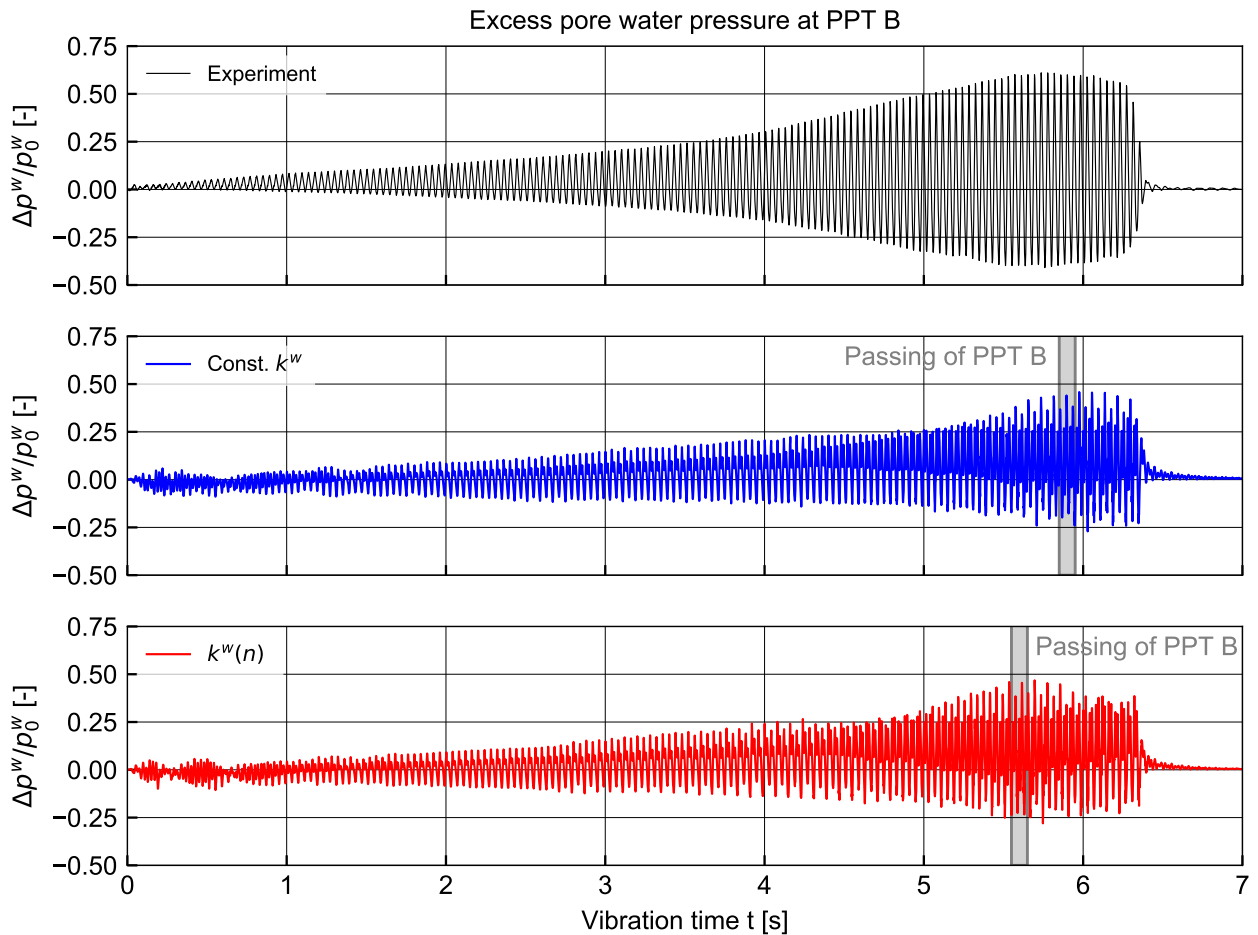


Figure 15: Normalised excess pore water pressure at PPT B (see Fig. 6) for the values measured in the experiment and the simulations using either a constant hydraulic conductivity k^w or the Kozeny/Carman equation ($k^w(n)$)

- 814 Berg, P. V. D. (1994). “Analysis of soil penetration”. PhD thesis. Delft University of Technology, pp. 133–
815 143.
- 816 Bienen, B., S. Fan, M. Schröder, and M. F. Randolph (Sept. 2021). “Effect of the installation process
817 on monopile lateral response”. In: *Proceedings of the Institution of Civil Engineers - Geotechnical*
818 *Engineering*, pp. 1–19. ISSN: 1353-2618. DOI: [10.1680/jgeen.20.00219](https://doi.org/10.1680/jgeen.20.00219). URL: <https://doi.org/10.1680/jgeen.20.00219>.
819 <https://www.icevirtuallibrary.com/doi/10.1680/jgeen.20.00219>.
- 820 Buczkowski, R. (1998). “21-Node hexahedral isoparametric element for analysis of contact problems”. In:
821 *Communications in Numerical Methods in Engineering* 14, pp. 681–692. DOI: [10.1002/\(SICI\)1099-0887\(199807\)14:7<681::AID-CNM182>3.0.CO;2-T](https://doi.org/10.1002/(SICI)1099-0887(199807)14:7<681::AID-CNM182>3.0.CO;2-T).
- 822 Buczkowski, R., M. Kieiber, and U. Gabbert (1994). “On linear and higher order standard finite elements
823 for 3D-nonlinear contact problem”. In: *Computers & Structures* 53.4, pp. 817–823. ISSN: 0045-7949.
824 DOI: [https://doi.org/10.1016/0045-7949\(94\)90370-0](https://doi.org/10.1016/0045-7949(94)90370-0).
- 825 Carman, P. C. (1939). “Permeability of saturated sands, soils and clays”. In: *The Journal of Agricultural*
826 *Science* 29.2, pp. 262–273. ISSN: 14695146. DOI: [10.1017/S0021859600051789](https://doi.org/10.1017/S0021859600051789).
- 827 Cerfontaine, B., A. C. Dieudonné, J. P. Radu, F. Collin, and R. Charlier (2015). “3D zero-thickness coupled
828 interface finite element: Formulation and application”. In: *Computers and Geotechnics* 69, pp. 124–
829 140. ISSN: 18737633. DOI: [10.1016/j.compgeo.2015.04.016](https://doi.org/10.1016/j.compgeo.2015.04.016). URL: <https://www.sciencedirect.com/science/article/pii/S0266352X15000956>.
830
831

- 832 Chrisopoulos, S. (2018). “Contributions to the Numerical Modelling of Vibratory Pile Driving in Saturated
833 Soil”. PhD thesis. Dissertation, Publications of the Institute of Soil Mechanics and Rock Mechanics,
834 Karlsruhe Institute of Technology, Issue No. 184.
- 835 Chrisopoulos, S., V. A. Osinov, and T. Triantafyllidis (2016). “Dynamic Problem for the Deformation of
836 Saturated Soil in the Vicinity of a Vibrating Pile Toe”. In: *Holistic Simulation of Geotechnical Instal-*
837 *lation Processes: Benchmarks and Simulations*. Ed. by T. Triantafyllidis. Cham: Springer International
838 Publishing, pp. 53–67. DOI: [10.1007/978-3-319-23159-4_3](https://doi.org/10.1007/978-3-319-23159-4_3). URL: [https://doi.org/10.1007/978-](https://doi.org/10.1007/978-3-319-23159-4_3)
839 [3-319-23159-4_3](https://doi.org/10.1007/978-3-319-23159-4_3).
- 840 Chrisopoulos, S. and J. Vogelsang (2019). “A finite element benchmark study based on experimental
841 modeling of vibratory pile driving in saturated sand”. In: *Soil Dynamics and Earthquake Engineering*
842 122, pp. 248–260. ISSN: 0267-7261. DOI: <https://doi.org/10.1016/j.soildyn.2019.01.001>.
- 843 Cui, W., D. M. Potts, L. Zdravković, K. A. Gawecka, and A. Tsiamposi (2019). “Formulation and
844 application of 3D THM-coupled zero-thickness interface elements”. In: *Computers and Geotechnics*
845 116, p. 103204. ISSN: 18737633. DOI: [10.1016/j.compgeo.2019.103204](https://doi.org/10.1016/j.compgeo.2019.103204). URL: <https://www.sciencedirect.com/science/article/pii/S0266352X1930268X>.
- 847 Dafalias, Y. F. and M. T. Manzari (2004). “Simple Plasticity Sand Model Accounting for Fabric Change
848 Effects”. In: *Journal of Engineering Mechanics* 130.6, pp. 622–634. ISSN: 0733-9399. DOI: [10.1061/](https://doi.org/10.1061/(asce)0733-9399(2004)130:6(622))
849 [\(asce\)0733-9399\(2004\)130:6\(622\)](https://doi.org/10.1061/(asce)0733-9399(2004)130:6(622)).
- 850 Daryaei, R., M. Bakroon, D. Aubram, and F. Rackwitz (2020). “Numerical evaluation of the soil behav-
851 ior during pipe-pile installation using impact and vibratory driving in sand”. In: *Soil Dynamics and*
852 *Earthquake Engineering* 134, p. 106177. ISSN: 02677261. DOI: [10.1016/j.soildyn.2020.106177](https://doi.org/10.1016/j.soildyn.2020.106177).
- 853 DeJong, J. T. and Z. J. Westgate (Nov. 2009). “Role of Initial State, Material Properties, and Confinement
854 Condition on Local and Global Soil-Structure Interface Behavior”. In: *Journal of Geotechnical and*
855 *Geoenvironmental Engineering* 135.11, pp. 1646–1660. ISSN: 1090-0241. DOI: [10.1061/\(asce\)1090-](https://doi.org/10.1061/(asce)1090-0241(2009)135:11(1646))
856 [0241\(2009\)135:11\(1646\)](https://doi.org/10.1061/(asce)1090-0241(2009)135:11(1646)).
- 857 DeJong, J. T., D. J. White, and M. F. Randolph (Feb. 2006). “Microscale Observation and Modeling of
858 Soil-Structure Interface Behavior Using Particle Image Velocimetry”. In: *Soils and Foundations* 46.1,
859 pp. 15–28. ISSN: 00380806. DOI: [10.3208/sandf.46.15](https://doi.org/10.3208/sandf.46.15). URL: [https://linkinghub.elsevier.com/](https://linkinghub.elsevier.com/retrieve/pii/S0038080620305473)
860 [retrieve/pii/S0038080620305473](https://linkinghub.elsevier.com/retrieve/pii/S0038080620305473).
- 861 Ehlers, W. and J. Bluhm (2013). *Porous Media: Theory, Experiments and Numerical Applications*.
862 Springer Berlin Heidelberg. ISBN: 9783662049990. URL: [https://books.google.de/books?id=](https://books.google.de/books?id=vbXoCAAQBAJ)
863 [vbXoCAAQBAJ](https://books.google.de/books?id=vbXoCAAQBAJ).
- 864 Fakharian, K. (1996). “Three Dimensional Monotonic and Cyclic Behaviour of sand-steel interfaces:
865 Testing and Modeling”. PhD thesis. University of Ottawa, pp. 1–283.
- 866 Falk, R. S. (1993). *Mixed and Hybrid Finite Element Methods (Franco Brezzi and Michel Fortin)*. Vol. 35.
867 3. Springer Science & Business Media, pp. 514–517. DOI: [10.1137/1035113](https://doi.org/10.1137/1035113).
- 868 Fan, S., B. Bienen, and M. F. Randolph (2021). “Effects of Monopile Installation on Subsequent Lateral
869 Response in Sand. I: Pile Installation”. In: *Journal of Geotechnical and Geoenvironmental Engineering*
870 147.5, p. 04021021. ISSN: 1090-0241. DOI: [10.1061/\(asce\)gt.1943-5606.0002467](https://doi.org/10.1061/(asce)gt.1943-5606.0002467).
- 871 Farah, P., W. A. Wall, and A. Popp (2018). “A mortar finite element approach for point, line, and surface
872 contact”. In: *International Journal for Numerical Methods in Engineering* 114.3, pp. 255–291. ISSN:
873 10970207. DOI: [10.1002/nme.5743](https://doi.org/10.1002/nme.5743).
- 874 Farah, P., A. Popp, and W. A. Wall (2015). “Segment-based vs. Element-based integration for mortar
875 methods in computational contact mechanics”. In: *Computational Mechanics* 55.1, pp. 209–228. ISSN:
876 01787675. DOI: [10.1007/s00466-014-1093-2](https://doi.org/10.1007/s00466-014-1093-2). URL: [https://doi.org/10.1007/s00466-014-1093-](https://doi.org/10.1007/s00466-014-1093-2)
877 [2](https://doi.org/10.1007/s00466-014-1093-2).
- 878 Feng, D. K., J. M. Zhang, and L. J. Deng (Mar. 2018). “Three-dimensional monotonic and cyclic behavior
879 of a gravel-steel interface from large-scale simple-shear tests”. In: *Canadian Geotechnical Journal* 55.11,
880 pp. 1657–1667. ISSN: 12086010. DOI: [10.1139/cgj-2018-0065](https://doi.org/10.1139/cgj-2018-0065). URL: [https://doi.org/10.1139/cgj-](https://doi.org/10.1139/cgj-2018-0065)
881 [2018-0065](https://doi.org/10.1139/cgj-2018-0065).

- 882 Fischer, K. A. and P. Wriggers (2005). “Frictionless 2D contact formulations for finite deformations
883 based on the mortar method”. In: *Computational Mechanics* 36.3, pp. 226–244. ISSN: 01787675. DOI:
884 [10.1007/s00466-005-0660-y](https://doi.org/10.1007/s00466-005-0660-y). URL: <https://doi.org/10.1007/s00466-005-0660-y>.
- 885 Fischer, K. A., D. Sheng, and A. J. Abbo (Nov. 2007). “Modeling of pile installation using contact
886 mechanics and quadratic elements”. In: *Computers and Geotechnics* 34.6, pp. 449–461. ISSN: 0266352X.
887 DOI: [10.1016/j.compgeo.2007.01.003](https://doi.org/10.1016/j.compgeo.2007.01.003).
- 888 Fischer, K. A. and P. Wriggers (2006). “Mortar based frictional contact formulation for higher order
889 interpolations using the moving friction cone”. In: *Computer Methods in Applied Mechanics and En-*
890 *gineering* 195.37-40, pp. 5020–5036. ISSN: 00457825. DOI: [10.1016/j.cma.2005.09.025](https://doi.org/10.1016/j.cma.2005.09.025). URL: <https://www.sciencedirect.com/science/article/pii/S0045782505005359>.
- 891 Galavi, V., M. Martinelli, A. Elkadi, P. Ghasemi, and R. Thijssen (2019). “Numerical simulation of impact
892 driven offshore monopiles using the material point method”. In: *Proceedings of the XVII ECSMGE-*
893 *2019*. DOI: [10.32075/17ECSMGE-2019-0758](https://doi.org/10.32075/17ECSMGE-2019-0758).
- 894 Ghionna, V. N. and G. Mortara (2002). “An elastoplastic model for sand-structure interface behaviour”.
895 In: *Geotechnique* 52.1, pp. 41–50. ISSN: 00168505. DOI: [10.1680/geot.2002.52.1.41](https://doi.org/10.1680/geot.2002.52.1.41). URL: <https://doi.org/10.1680/geot.2002.52.1.41>.
- 896 Ghorbani, J., M. Nazem, J. Kodikara, and P. Wriggers (2021). “Finite element solution for static and
897 dynamic interactions of cylindrical rigid objects and unsaturated granular soils”. In: *Computer Methods*
898 *in Applied Mechanics and Engineering* 384, p. 113974. ISSN: 0045-7825. DOI: [https://doi.org/10.](https://doi.org/10.1016/j.cma.2021.113974)
899 [1016/j.cma.2021.113974](https://doi.org/10.1016/j.cma.2021.113974). URL: [https://www.sciencedirect.com/science/article/pii/](https://www.sciencedirect.com/science/article/pii/S0045782521003054)
900 [S0045782521003054](https://www.sciencedirect.com/science/article/pii/S0045782521003054).
- 901 Grabe, J. and K.-P. Mahutka (2005). “Finite-Elemente-Analyse zur Vibrationsrammung von Pfählen”.
902 In: *Bautechnik* 82.9, pp. 632–640. ISSN: 1437-0999. DOI: [10.1002/bate.200590192](https://doi.org/10.1002/bate.200590192). URL: <http://dx.doi.org/10.1002/bate.200590192>.
- 903 Gutjahr, S. (Oct. 2003). “Optimierte Berechnung von nicht gestützten Baugrubenwänden in Sand”. PhD
904 thesis. Universität Dortmund.
- 905 Habraken, A. M. and S. Cescotto (1998). “Contact between deformable solids: The fully coupled ap-
906 proach”. In: *Mathematical and Computer Modelling* 28.4-8, pp. 153–169. ISSN: 08957177. DOI: [10.](https://doi.org/10.1016/S0895-7177(98)00115-0)
907 [1016/S0895-7177\(98\)00115-0](https://doi.org/10.1016/S0895-7177(98)00115-0). URL: [https://www.sciencedirect.com/science/article/pii/](https://www.sciencedirect.com/science/article/pii/S0895717798001150)
908 [S0895717798001150](https://www.sciencedirect.com/science/article/pii/S0895717798001150).
- 909 Heins, E., M. F. Randolph, B. Bienen, and J. Grabe (2020). “Effect of installation method on static
910 and dynamic load test response for piles in sand”. In: *International Journal of Physical Modelling in*
911 *Geotechnics* 20.1, pp. 1–23. ISSN: 20426550. DOI: [10.1680/jphmg.18.00028](https://doi.org/10.1680/jphmg.18.00028). URL: [https://doi.org/](https://doi.org/10.1680/jphmg.18.00028)
912 [10.1680/jphmg.18.00028](https://doi.org/10.1680/jphmg.18.00028).
- 913 Henke, S. and J. Grabe (2008). “Numerical investigation of soil plugging inside open-ended piles with
914 respect to the installation method”. In: *Acta Geotechnica* 3.3, pp. 215–223.
- 915 Henke, S. (Aug. 2010). “Influence of pile installation on adjacent structures”. In: *International Journal*
916 *for Numerical and Analytical Methods in Geomechanics* 34.11, pp. 1191–1210. ISSN: 03639061. DOI:
917 [10.1002/nag.859](https://doi.org/10.1002/nag.859). URL: <https://doi.org/10.1002/nag.859>.
- 918 Henke, S. (2014). “Untersuchungen zur Pfropfenbildung infolge der Installation offener Profile in gran-
919 ularen Böden”. Habilitation. Hamburg-Harburg: Veröffentlichungen des Instituts für Geotechnik und
920 Baubetrieb.
- 921 Henke, S., Grabe, J. (2008). “Numerische Untersuchungen zur Pfropfenbildung in offenen Profilen in
922 Abhängigkeit des Einbringverfahrens”. In: *Bautechnik* 85.8, pp. 521–529.
- 923 Herle, I. and K. Nübel (1999). “Hypoplastic description of the interface behaviour”. In: *Numerical models*
924 *in geomechanics. Proceedings of the 7th international symposium, Graz, September 1999*. Ed. by G.
925 Pande, S. Pietruszczak, and H. Schweiger, pp. 53–58. ISBN: 9058090957.
- 926 Hesch, C. and P. Betsch (2011). “Transient three-dimensional contact problems: Mortar method. Mixed
927 methods and conserving integration”. In: *Computational Mechanics* 48.4, pp. 461–475. ISSN: 01787675.
928 DOI: [10.1007/s00466-011-0583-8](https://doi.org/10.1007/s00466-011-0583-8). URL: <https://doi.org/10.1007/s00466-011-0583-8>.
- 929
930
931

- 932 Hilber, H. M., T. J. Hughes, and R. L. Taylor (1977). “Improved numerical dissipation for time integration
933 algorithms in structural dynamics”. In: *Earthquake Engineering & Structural Dynamics* 5.3, pp. 283–
934 292. ISSN: 10969845. DOI: [10.1002/eqe.4290050306](https://doi.org/10.1002/eqe.4290050306).
- 935 Hu, L. and J. Pu (Aug. 2004). “Testing and Modeling of Soil-Structure Interface”. In: *Journal of Geotech-
936 nical and Geoenvironmental Engineering* 130.8, pp. 851–860. ISSN: 1090-0241. DOI: [10.1061/\(asce\)
937 1090-0241\(2004\)130:8\(851\)](https://doi.org/10.1061/(asce)1090-0241(2004)130:8(851)). URL: [https://doi.org/10.1061/\(ASCE\)1090-0241\(2004\)130:
938 8\(851\)](https://doi.org/10.1061/(ASCE)1090-0241(2004)130:8(851)).
- 939 Hughes, T. J. and J. Winget (1980). “Finite rotation effects in numerical integration of rate constitutive
940 equations arising in large deformation analysis”. In: *International Journal for Numerical Methods in
941 Engineering* 15.12, pp. 1862–1867. ISSN: 10970207. DOI: [10.1002/nme.1620151210](https://doi.org/10.1002/nme.1620151210).
- 942 Idelsohn, S. R., E. Onate, and F. Del Pin (2004). “The particle finite element method: A powerful tool
943 to solve incompressible flows with free-surfaces and breaking waves”. In: *International Journal for
944 Numerical Methods in Engineering* 61.7, pp. 964–989. ISSN: 00295981. DOI: [10.1002/nme.1096](https://doi.org/10.1002/nme.1096).
- 945 Johnson, K. L. (1987). *Contact Mechanics*. Cambridge University Press. ISBN: 9780521347969. URL:
946 <https://books.google.de/books?id=Do6WQlUwbpkC>.
- 947 Kozeny Josef (1927). *Über kapillare Leitung des Wassers im Boden*. Vol. 136. 2a. Hölder-Pichler-Tempsky,
948 A.-G.[Abt.]: Akad. d. Wiss., pp. 271–306. URL: www.biologiezentrum.at.
- 949 Lashkari, A. (2012). “A plasticity model for sand-structure interfaces”. In: *Journal of Central South
950 University of Technology (English Edition)* 19.4, pp. 1098–1108. ISSN: 10059784. DOI: [10.1007/s11771-
951 012-1115-1](https://doi.org/10.1007/s11771-012-1115-1). URL: <https://doi.org/10.1007/s11771-012-1115-1>.
- 952 Laursen, T. A., M. A. Puso, and J. Sanders (2012). “Mortar contact formulations for deformable-
953 deformable contact: Past contributions and new extensions for enriched and embedded interface for-
954 mulations”. In: *Computer Methods in Applied Mechanics and Engineering* 205-208.1, pp. 3–15. ISSN:
955 00457825. DOI: [10.1016/j.cma.2010.09.006](https://doi.org/10.1016/j.cma.2010.09.006). URL: [https://www.sciencedirect.com/science/
956 article/pii/S0045782510002653](https://www.sciencedirect.com/science/article/pii/S0045782510002653).
- 957 Le, V. H., F. Remspecher, and F. Rackwitz (2021). “Development of numerical models for the long-term
958 behaviour of monopile foundations under cyclic loading considering the installation effects”. In: *Soil
959 Dynamics and Earthquake Engineering* 150, p. 106927. ISSN: 02677261. DOI: [10.1016/j.soildyn.
960 2021.106927](https://doi.org/10.1016/j.soildyn.2021.106927). URL: <https://www.sciencedirect.com/science/article/pii/S0267726121003493>.
- 961 Li, C., R. I. Borja, and R. A. Regueiro (2004). “Dynamics of porous media at finite strain”. In: *Computer
962 Methods in Applied Mechanics and Engineering* 193.36, pp. 3837–3870. ISSN: 0045-7825.
- 963 Liu, H. and H. I. Ling (2008). “Constitutive description of interface behavior including cyclic loading
964 and particle breakage within the framework of critical state soil mechanics”. In: *International Journal
965 for Numerical and Analytical Methods in Geomechanics* 32.12, pp. 1495–1514. ISSN: 03639061. DOI:
966 [10.1002/nag.682](https://doi.org/10.1002/nag.682). URL: <https://onlinelibrary.wiley.com/doi/abs/10.1002/nag.682>.
- 967 Liu, H., E. Song, and H. I. Ling (2006). “Constitutive modeling of soil-structure interface through the
968 concept of critical state soil mechanics”. In: *Mechanics Research Communications* 33.4, pp. 515–531.
969 ISSN: 00936413. DOI: [10.1016/j.mechrescom.2006.01.002](https://doi.org/10.1016/j.mechrescom.2006.01.002). URL: [https://www.sciencedirect.
970 com/science/article/pii/S0093641306000048](https://www.sciencedirect.com/science/article/pii/S0093641306000048).
- 971 Liu, J., D. Zou, and X. Kong (Sept. 2014). “A three-dimensional state-dependent model of soil-structure
972 interface for monotonic and cyclic loadings”. In: *Computers and Geotechnics* 61, pp. 166–177. ISSN:
973 0266352X. DOI: [10.1016/j.compgeo.2014.05.012](https://doi.org/10.1016/j.compgeo.2014.05.012).
- 974 Macháček, J. and P. Staubach (2021). “numgeo: A finite-element program for the simulation of hydro-
975 mechanically coupled geotechnical processes”. In: *Fachsektionstage Geotechnik 2021*. DGGT. URL:
976 <https://www.numgeo.de/wp-content/uploads/2022/01/numgeoMachacekStaubachFSTB2021.pdf>.
- 977 Macháček, J., P. Staubach, M. Tafili, H. Zachert, and T. Wichtmann (2021a). “Performance of different
978 constitutive soil models: from element tests to the simulation of vibratory pile driving tests”. In:
979 *XVI International Conference on Computational Plasticity. Fundamentals and Applications COMPLAS
980 2021*.
- 981 Macháček, J., P. Staubach, M. Tafili, H. Zachert, and T. Wichtmann (2021b). “Investigation of three
982 sophisticated constitutive soil models: From numerical formulations to element tests and the analysis

- 983 of vibratory pile driving tests”. In: *Computers and Geotechnics* 138, p. 104276. ISSN: 18737633. DOI:
984 [10.1016/j.compgeo.2021.104276](https://doi.org/10.1016/j.compgeo.2021.104276).
- 985 Machaček, J. (2020). *Contributions to the Numerical Modelling of Saturated and Unsaturated Soils*. Dis-
986 sertation, Publications of the Institute of Soil Mechanics and Rock Mechanics, Karlsruhe Institute of
987 Technology, Issue No. 187.
- 988 Martinez, A., J. D. Frost, and G. L. Hebel (July 2015). “Experimental study of shear zones formed
989 at sand/steel interfaces in axial and torsional axisymmetric tests”. In: *Geotechnical Testing Journal*
990 38.4, pp. 409–426. ISSN: 01496115. DOI: [10.1520/GTJ20140266](https://doi.org/10.1520/GTJ20140266). URL: [https://compass.astm.org/
991 DIGITAL%7B%5C_%7DLIBRARY/JOURNALS/GEOTECH/PAGES/GTJ20140266.htm](https://compass.astm.org/DIGITAL%7B%5C_%7DLIBRARY/JOURNALS/GEOTECH/PAGES/GTJ20140266.htm).
- 992 Moormann, C., S. Gowda, and S. Giridharan (2019). “Numerical simulation of open ended pile installation
993 in saturated sand”. In: *Springer Series in Geomechanics and Geoengineering*. Ed. by A. Ferrari and L.
994 Laloui. Vol. 0. 217729. Cham: Springer International Publishing, pp. 459–466. ISBN: 978-3-319-99670-7.
995 DOI: [10.1007/978-3-319-99670-7_57](https://doi.org/10.1007/978-3-319-99670-7_57).
- 996 Niemunis, A. and I. Herle (1997). “Hypoplastic model for cohesionless soils with elastic strain range”. In:
997 *Mechanics of Cohesive-Frictional Materials* 2.4, pp. 279–299. ISSN: 10825010. DOI: [10.1002/\(SICI\)
998 1099-1484\(199710\)2:4<279::AID-CFM29>3.0.CO;2-8](https://doi.org/10.1002/(SICI)1099-1484(199710)2:4<279::AID-CFM29>3.0.CO;2-8). URL: [http://dx.doi.org/10.1002/\(SICI\)
999 1099-1484\(199710\)2:4%7B%5C%7D3C279::AID-CFM29%7B%5C%7D3E3.0.CO;2-8](http://dx.doi.org/10.1002/(SICI)1099-1484(199710)2:4%7B%5C%7D3C279::AID-CFM29%7B%5C%7D3E3.0.CO;2-8).
- 1000 Osinov, V. A. (2015). “Numerical Modelling of the Effective-Stress Evolution in Saturated Soil Around
1001 a Vibrating Pile Toe”. In: *Holistic Simulation of Geotechnical Installation Processes: Numerical and
1002 Physical Modelling*. Ed. by T. Triantafyllidis. Cham: Springer International Publishing, pp. 133–147.
1003 ISBN: 978-3-319-18170-7. DOI: [10.1007/978-3-319-18170-7_7](https://doi.org/10.1007/978-3-319-18170-7_7). URL: [https://doi.org/10.1007/
1004 978-3-319-18170-7_7](https://doi.org/10.1007/978-3-319-18170-7_7).
- 1005 Osinov, V. A., S. Chrisopoulos, and T. Triantafyllidis (Aug. 2013). “Numerical study of the deformation of
1006 saturated soil in the vicinity of a vibrating pile”. In: *Acta Geotechnica* 8.4, pp. 439–446. ISSN: 1861-1133.
1007 DOI: [10.1007/s11440-012-0190-7](https://doi.org/10.1007/s11440-012-0190-7). URL: <https://doi.org/10.1007/s11440-012-0190-7>.
- 1008 Papadopoulos, P. and R. L. Taylor (1992). “A mixed formulation for the finite element solution of contact
1009 problems”. In: *Computer Methods in Applied Mechanics and Engineering* 94.3, pp. 373–389. ISSN:
1010 00457825. DOI: [10.1016/0045-7825\(92\)90061-N](https://doi.org/10.1016/0045-7825(92)90061-N). URL: [https://www.sciencedirect.com/science/
1011 article/pii/004578259290061N](https://www.sciencedirect.com/science/article/pii/004578259290061N).
- 1012 Popov, V. L. (2009). *Kontaktmechanik und Reibung: ein Lehr- und Anwendungsbuch von der Nanotri-
1013 bologie bis zur numerischen Simulation*. Springer. ISBN: 9783540888369. URL: [https://books.google.
1014 de/books?id=umh20zHZTX4C](https://books.google.de/books?id=umh20zHZTX4C).
- 1015 Popp, A. (2012). “Mortar Methods for Computational Contact Mechanics and General Interface Probl-
1016 ems”. Dissertation. München: Technische Universität München.
- 1017 Popp, A., M. W. Gee, and W. A. Wall (2009). “A finite deformation mortar contact formulation using a
1018 primal-dual active set strategy”. In: *International Journal for Numerical Methods in Engineering* 79.11,
1019 pp. 1354–1391. ISSN: 00295981. DOI: [10.1002/nme.2614](https://doi.org/10.1002/nme.2614). URL: [https://onlinelibrary.wiley.com/
1020 doi/abs/10.1002/nme.2614](https://onlinelibrary.wiley.com/doi/abs/10.1002/nme.2614).
- 1021 Popp, A., M. Gitterle, M. W. Gee, and W. A. Wall (2010). “A dual mortar approach for 3D finite
1022 deformation contact with consistent linearization”. In: *International Journal for Numerical Methods
1023 in Engineering* 83.11, pp. 1428–1465. ISSN: 00295981. DOI: [10.1002/nme.2866](https://doi.org/10.1002/nme.2866). URL: [https://
1024 onlinelibrary.wiley.com/doi/abs/10.1002/nme.2866](https://onlinelibrary.wiley.com/doi/abs/10.1002/nme.2866).
- 1025 Puso, M. A. and T. A. Laursen (Nov. 2004). “A mortar segment-to-segment frictional contact method for
1026 large deformations”. In: *Computer Methods in Applied Mechanics and Engineering* 193.45-47, pp. 4891–
1027 4913. ISSN: 00457825. DOI: [10.1016/j.cma.2004.06.001](https://doi.org/10.1016/j.cma.2004.06.001). URL: [http://www.sciencedirect.com/
1028 science/article/pii/S0045782504002518](http://www.sciencedirect.com/science/article/pii/S0045782504002518)[https://linkinghub.elsevier.com/retrieve/
1029 pii/S0045782504002518](https://linkinghub.elsevier.com/retrieve/pii/S0045782504002518).
- 1030 Puso, M. A., T. A. Laursen, and J. Solberg (2008). “A segment-to-segment mortar contact method
1031 for quadratic elements and large deformations”. In: *Computer Methods in Applied Mechanics and
1032 Engineering* 197.6-8, pp. 555–566. ISSN: 00457825. DOI: [10.1016/j.cma.2007.08.009](https://doi.org/10.1016/j.cma.2007.08.009).

- 1033 Saberi, M., C. D. Annan, and J. M. Konrad (2018). “On the mechanics and modeling of interfaces
1034 between granular soils and structural materials”. In: *Archives of Civil and Mechanical Engineering*
1035 18.4, pp. 1562–1579. ISSN: 16449665. DOI: [10.1016/j.acme.2018.06.003](https://doi.org/10.1016/j.acme.2018.06.003).
- 1036 Saberi, M., C. D. Annan, and J. M. Konrad (July 2020). “Three-dimensional constitutive model for cyclic
1037 behavior of soil-structure interfaces”. In: *Soil Dynamics and Earthquake Engineering* 134, p. 106162.
1038 ISSN: 02677261. DOI: [10.1016/j.soildyn.2020.106162](https://doi.org/10.1016/j.soildyn.2020.106162).
- 1039 Saberi, M., C. D. Annan, J. M. Konrad, and A. Lashkari (2016). “A critical state two-surface plasticity
1040 model for gravelly soil-structure interfaces under monotonic and cyclic loading”. In: *Computers and*
1041 *Geotechnics* 80, pp. 71–82. ISSN: 18737633. DOI: [10.1016/j.compgeo.2016.06.011](https://doi.org/10.1016/j.compgeo.2016.06.011). URL: <https://www.sciencedirect.com/science/article/pii/S0266352X16301380>.
- 1043 Sabetamal, H., J. P. Carter, M. Nazem, and S. W. Sloan (July 2016a). “Coupled analysis of dynamically
1044 penetrating anchors”. In: *Computers and Geotechnics* 77, pp. 26–44. ISSN: 18737633. DOI: [10.1016/j.compgeo.2016.04.005](https://doi.org/10.1016/j.compgeo.2016.04.005).
- 1046 Sabetamal, H., M. Nazem, S. W. Sloan, and J. P. Carter (Jan. 2016b). “Frictionless contact formulation for
1047 dynamic analysis of nonlinear saturated porous media based on the mortar method”. In: *International*
1048 *Journal for Numerical and Analytical Methods in Geomechanics* 40.1, pp. 25–61. ISSN: 10969853. DOI:
1049 [10.1002/nag.2386](https://doi.org/10.1002/nag.2386). URL: <https://doi.org/10.1002/nag.2386>.
- 1050 Schrefler, B. A., L. Simoni, L. Xikui, and O. C. Zienkiewicz (1990). *Mechanics of Partially Saturated*
1051 *Porous Media*. Springer Vienna.
- 1052 Segura, J. M. and I. Carol (2008). “Coupled HM analysis using zero-thickness interface elements with
1053 double nodes. Part I: Theoretical model”. In: *International Journal for Numerical and Analytical Meth-*
1054 *ods in Geomechanics* 32.18, pp. 2083–2101. DOI: <https://doi.org/10.1002/nag.735>. URL: <https://onlinelibrary.wiley.com/doi/abs/10.1002/nag.735>.
- 1056 Sheng, D., K. D. Eigenbrod, and P. Wriggers (2005). “Finite element analysis of pile installation using
1057 large-slip frictional contact”. In: *Computers and Geotechnics* 32.1, pp. 17–26. ISSN: 0266-352X. DOI:
1058 <https://doi.org/10.1016/j.compgeo.2004.10.004>. URL: <https://www.sciencedirect.com/science/article/pii/S0266352X04001326>.
- 1060 Simo, J. C., P. Wriggers, and R. L. Taylor (1985). “A perturbed Lagrangian formulation for the finite
1061 element solution of contact problems”. In: *Computer Methods in Applied Mechanics and Engineering*
1062 50.2, pp. 163–180. ISSN: 00457825. DOI: [10.1016/0045-7825\(85\)90088-X](https://doi.org/10.1016/0045-7825(85)90088-X).
- 1063 Sitzmann, S. (2016). “Robust Algorithms for Contact Problems with Constitutive Contact Laws”. PhD
1064 thesis. Friedrich-Alexander-Universität Erlangen-Nürnberg, p. 144.
- 1065 Soleimani, M. and C. Weissenfels (2021). “Numerical simulation of pile installations in a hypoplastic
1066 framework using an SPH based method”. In: *Computers and Geotechnics* 133, p. 104006. ISSN: 0266-
1067 352X. DOI: <https://doi.org/10.1016/j.compgeo.2021.104006>.
- 1068 Sorensen, E. S., J. Clausen, and L. Damkilde (Mar. 2017). “Comparison of numerical formulations for
1069 the modeling of tensile loaded suction buckets”. In: *Computers and Geotechnics* 83, pp. 198–208. ISSN:
1070 18737633. DOI: [10.1016/j.compgeo.2016.10.026](https://doi.org/10.1016/j.compgeo.2016.10.026).
- 1071 Staubach, P. and J. Macháček (Aug. 2019). “Influence of relative acceleration in saturated sand: Analytical
1072 approach and simulation of vibratory pile driving tests”. In: *Computers and Geotechnics* 112, pp. 173–
1073 184. ISSN: 0266352X. DOI: [10.1016/j.compgeo.2019.03.027](https://doi.org/10.1016/j.compgeo.2019.03.027). URL: <https://linkinghub.elsevier.com/retrieve/pii/S0266352X19301028>.
- 1074 Staubach, P., J. Macháček, R. Sharif, and T. Wichtmann (June 2021a). “Back-analysis of model tests
1075 on piles in sand subjected to long-term lateral cyclic loading: Impact of the pile installation and
1076 application of the HCA model”. In: *Computers and Geotechnics* 134, p. 104018. ISSN: 0266352X. DOI:
1077 [10.1016/j.compgeo.2021.104018](https://doi.org/10.1016/j.compgeo.2021.104018). URL: <https://linkinghub.elsevier.com/retrieve/pii/S0266352X21000215>.
- 1080 Staubach, P., J. Macháček, M. C. Moscoso, and T. Wichtmann (2020). “Impact of the installation on
1081 the long-term cyclic behaviour of piles in sand: A numerical study”. In: *Soil Dynamics and Earthquake*
1082 *Engineering* 138, p. 106223. ISSN: 02677261. DOI: [10.1016/j.soildyn.2020.106223](https://doi.org/10.1016/j.soildyn.2020.106223).

- 1083 Staubach, P., J. Machaček, J. Skowronek, and T. Wichtmann (Feb. 2021b). “Vibratory pile driving in
1084 water-saturated sand: Back-analysis of model tests using a hydro-mechanically coupled CEL method”.
1085 In: *Soils and Foundations* 61.1, pp. 144–159. ISSN: 00380806. DOI: [10.1016/j.sandf.2020.11.005](https://doi.org/10.1016/j.sandf.2020.11.005).
- 1086 Staubach, P., J. Machaček, L. Tschirschky, and T. Wichtmann (Feb. 2022a). “Enhancement of a high-
1087 cycle accumulation model by an adaptive strain amplitude and its application to monopile foundations”.
1088 In: *International Journal for Numerical and Analytical Methods in Geomechanics* 46.2, pp. 315–338.
1089 ISSN: 0363-9061. DOI: [10.1002/nag.3301](https://doi.org/10.1002/nag.3301). URL: <https://onlinelibrary.wiley.com/doi/10.1002/nag.3301>.
- 1090 Staubach, P., J. Machaček, M. Tafili, and T. Wichtmann (Jan. 2022b). “A high-cycle accumulation
1091 model for clay and its application to monopile foundations”. In: *Acta Geotechnica*. ISSN: 1861-1125.
1092 DOI: [10.1007/s11440-021-01446-9](https://doi.org/10.1007/s11440-021-01446-9). URL: <https://link.springer.com/10.1007/s11440-021-01446-9>.
- 1093 Staubach, P., J. Machaček, and T. Wichtmann (Dec. 2021c). “Large-deformation analysis of pile installa-
1094 tion with subsequent lateral loading: Sanisand vs. Hypoplasticity”. In: *Soil Dynamics and Earthquake*
1095 *Engineering* 151, p. 106964. ISSN: 02677261. DOI: [10.1016/j.soildyn.2021.106964](https://doi.org/10.1016/j.soildyn.2021.106964). URL: <https://linkinghub.elsevier.com/retrieve/pii/S0267726121003869>.
- 1096 Staubach, P., J. Machaček, and T. Wichtmann (Feb. 2022c). “Novel approach to apply existing constitu-
1097 tive soil models to the modelling of interfaces”. In: *International Journal for Numerical and Analytical*
1098 *Methods in Geomechanics*. ISSN: 0363-9061. DOI: [10.1002/nag.3344](https://doi.org/10.1002/nag.3344). URL: <https://onlinelibrary.wiley.com/doi/10.1002/nag.3344>.
- 1099 Stutz, H., D. Mašín, A. S. Sattari, and F. Wuttke (July 2017). “A general approach to model interfaces
1100 using existing soil constitutive models application to hypoplasticity”. In: *Computers and Geotechnics*
1101 87, pp. 115–127. ISSN: 18737633. DOI: [10.1016/j.compgeo.2017.02.010](https://doi.org/10.1016/j.compgeo.2017.02.010).
- 1102 Stutz, H., D. Mašín, and F. Wuttke (2016). “Enhancement of a hypoplastic model for granular soil-
1103 structure interface behaviour”. In: *Acta Geotechnica* 11.6, pp. 1249–1261. ISSN: 18611133. DOI: [10.1007/s11440-016-0440-1](https://doi.org/10.1007/s11440-016-0440-1).
- 1104 Stutz, H. H. and F. Wuttke (Aug. 2018). “Hypoplastic modeling of soil-structure interfaces in offshore
1105 applications”. In: *Journal of Zhejiang University: Science A* 19.8, pp. 624–637. ISSN: 18621775. DOI:
1106 [10.1631/jzus.A1700469](https://doi.org/10.1631/jzus.A1700469). URL: <http://link.springer.com/10.1631/jzus.A1700469>.
- 1107 Stutz, H. and D. Mašín (2017). “Hypoplastic interface models for fine-grained soils”. In: *International*
1108 *Journal for Numerical and Analytical Methods in Geomechanics* 41.2, pp. 284–303. ISSN: 10969853.
1109 DOI: [10.1002/nag.2561](https://doi.org/10.1002/nag.2561).
- 1110 Sutherland, I. E. and G. W. Hodgman (1974). “Reentrant Polygon Clipping”. In: *Communications of the*
1111 *ACM* 17.1, pp. 32–42. ISSN: 15577317. DOI: [10.1145/360767.360802](https://doi.org/10.1145/360767.360802). URL: <https://doi.org/10.1145/360767.360802>.
- 1112 Taylor, C. and P. Hood (1973). “A numerical solution of the Navier-Stokes equations using the fi-
1113 nite element technique”. In: *Computers and Fluids* 1.1, pp. 73–100. ISSN: 00457930. DOI: [10.1016/0045-7930\(73\)90027-3](https://doi.org/10.1016/0045-7930(73)90027-3). URL: <https://www.sciencedirect.com/science/article/pii/S0045793073900273>.
- 1114 Tur, M., F. J. Fuenmayor, and P. Wriggers (2009). “A mortar-based frictional contact formulation for large
1115 deformations using Lagrange multipliers”. In: *Computer Methods in Applied Mechanics and Engineering*
1116 198.37, pp. 2860–2873. ISSN: 0045-7825. DOI: <https://doi.org/10.1016/j.cma.2009.04.007>. URL:
1117 <http://www.sciencedirect.com/science/article/pii/S0045782509001595>.
- 1118 Vogelsang, J., G. Huber, T. Triantafyllidis, and Bender (2015). “Interpretation of vibratory pile penetra-
1119 tion based on Digital Image Correlation”. In: *Springer International Publishing Switzerland*, pp. 31–
1120 51.
- 1121 Vogelsang, J. (2016). “Untersuchungen zu den Mechanismen der Pfahlrammung”. PhD thesis. Veröffentlichung
1122 des Instituts für Bodenmechanik und Felsmechanik am Karlsruher Institut für Technologie (KIT), Heft
1123 182.
- 1124 Vogelsang, J., G. Huber, and T. Triantafyllidis (2017). “Experimental Investigation of Vibratory Pile
1125 Driving in Saturated Sand”. In: *Holistic Simulation of Geotechnical Installation Processes: Theoretical*
1126 *Results and Applications*. Ed. by T. Triantafyllidis. Cham: Springer International Publishing, pp. 101–
1127 1128

- 1135 123. ISBN: 978-3-319-52590-7. DOI: [10.1007/978-3-319-52590-7_4](https://doi.org/10.1007/978-3-319-52590-7_4). URL: https://doi.org/10.1007/978-3-319-52590-7_4.
- 1136
- 1137 Weißenfels, C. and P. Wriggers (2015). “Methods to project plasticity models onto the contact surface
1138 applied to soil structure interactions”. In: *Computers and Geotechnics* 65, pp. 187–198. ISSN: 0266-352X.
1139 DOI: <https://doi.org/10.1016/j.compgeo.2014.11.015>. URL: <http://www.sciencedirect.com/science/article/pii/S0266352X14002201>.
- 1140
- 1141 Weißenfels, C., A. B. Harish, and P. Wriggers (2017). “Strategies to Apply Soil Models Directly as
1142 Friction Laws in Soil Structure Interactions”. In: *Holistic Simulation of Geotechnical Installation Pro-
1143 cesses: Theoretical Results and Applications*. Ed. by T. Triantafyllidis. Cham: Springer International
1144 Publishing, pp. 216–236. ISBN: 978-3-319-52590-7. DOI: [10.1007/978-3-319-52590-7_9](https://doi.org/10.1007/978-3-319-52590-7_9). URL:
1145 https://doi.org/10.1007/978-3-319-52590-7_9.
- 1146 Wohlmuth, B. I. (2001). *Iterative Solvers Based on Domain Decomposition*. Springer-Verlag Berlin Hei-
1147 delberg, pp. 85–176. ISBN: 354041083X. DOI: [10.1007/978-3-642-56767-4_2](https://doi.org/10.1007/978-3-642-56767-4_2).
- 1148 Wolffersorff, P. von (1996). “A hypoplastic relation for granular materials with a predefined limit state
1149 surface”. In: *Mechnics of Cohesive-Frictional Materials*.
- 1150 Wriggers, P. (2006a). *Computational Contact Mechanics*. Springer Berlin Heidelberg. ISBN: 9783540326090.
1151 URL: <https://books.google.de/books?id=oBMB4eMYsQC>.
- 1152 Wriggers, P. (2006b). *Computational contact mechanics*. Vol. 67. Lecture Notes in Applied and Compu-
1153 tational Mechanics. Berlin, Heidelberg: Springer Berlin Heidelberg, pp. 1–518. ISBN: 3540326081. DOI:
1154 [10.1007/978-3-540-32609-0](https://doi.org/10.1007/978-3-540-32609-0). URL: <http://link.springer.com/10.1007/978-3-642-31531-2>.
- 1155 Yang, B. and T. A. Laursen (Jan. 2008). “A large deformation mortar formulation of self contact with
1156 finite sliding”. In: *Computer Methods in Applied Mechanics and Engineering* 197.6-8, pp. 756–772. ISSN:
1157 00457825. DOI: [10.1016/j.cma.2007.09.004](https://doi.org/10.1016/j.cma.2007.09.004). URL: [https://linkinghub.elsevier.com/retrieve/
1158 pii/S0045782507003751](https://linkinghub.elsevier.com/retrieve/pii/S0045782507003751).
- 1159 Yang, B., T. A. Laursen, and X. Meng (Mar. 2005). “Two dimensional mortar contact methods for large
1160 deformation frictional sliding”. In: *International Journal for Numerical Methods in Engineering* 62.9,
1161 pp. 1183–1225. ISSN: 00295981. DOI: [10.1002/nme.1222](https://doi.org/10.1002/nme.1222). URL: [https://onlinelibrary.wiley.com/
1162 doi/abs/10.1002/nme.1222](https://onlinelibrary.wiley.com/doi/abs/10.1002/nme.1222) <https://onlinelibrary.wiley.com/doi/10.1002/nme.1222>.
- 1163 Yang, J. and Z. Y. Yin (July 2021). “Soil-structure interface modeling with the nonlinear incremental
1164 approach”. In: *International Journal for Numerical and Analytical Methods in Geomechanics* 45.10,
1165 pp. 1381–1404. ISSN: 10969853. DOI: [10.1002/nag.3206](https://doi.org/10.1002/nag.3206). URL: <https://doi.org/10.1002/nag.3206>.
- 1166 Yang, Z. X., Y. Y. Gao, R. J. Jardine, W. B. Guo, and D. Wang (2020). “Large Deformation Finite-
1167 Element Simulation of Displacement-Pile Installation Experiments in Sand”. In: *Journal of Geotechnical
1168 and Geoenvironmental Engineering* 146.6, p. 4020044. DOI: [10.1061/\(ASCE\)GT.1943-5606.0002271](https://doi.org/10.1061/(ASCE)GT.1943-5606.0002271).
- 1169 Zavarise, G. and P. Wriggers (1998). “A segment-to-segment contact strategy”. In: *Mathematical and
1170 Computer Modelling* 28.4-8, pp. 497–515. ISSN: 08957177. DOI: [10.1016/S0895-7177\(98\)00138-1](https://doi.org/10.1016/S0895-7177(98)00138-1).
- 1171 Zhang, G. and J.-M. Zhang (2008). “Unified Modeling of Monotonic and Cyclic Behavior of Interface
1172 between Structure and Gravelly Soil”. In: *Soils and Foundations* 48.2, pp. 231–245.
- 1173 Zhang, G. and J. M. Zhang (Feb. 2009). “Large-scale monotonic and cyclic tests of interface between
1174 geotextile and gravelly soil”. In: *Soils and Foundations* 49.1, pp. 75–84. ISSN: 00380806. DOI: [10.3208/
1175 sandf.49.75](https://doi.org/10.3208/sandf.49.75).
- 1176 Zienkiewicz, O. C. and T. Shiomi (1984). “Dynamic behaviour of saturated porous media: The generalized
1177 Biot formulation and its numerical solution”. In: *International Journal for Numerical and Analytical
1178 Methods in Geomechanics* 8.1, pp. 71–96. ISSN: 1096-9853. DOI: [10.1002/nag.1610080106](https://doi.org/10.1002/nag.1610080106). URL:
1179 <http://dx.doi.org/10.1002/nag.1610080106>.